

# 1 **AKAP79 enables calcineurin to directly suppress protein kinase A activity**

2

3 Timothy W. Church<sup>a</sup>, Parul Tewatia<sup>b,c</sup>, Saad Hannan<sup>a</sup>, João Antunes<sup>b</sup>, Olivia Eriksson<sup>b</sup>, Trevor G. Smart<sup>a</sup>,  
4 Jeanette Hellgren Kotaleski<sup>b,c</sup>, Matthew G. Gold<sup>a,1</sup>

5

6

7 <sup>a</sup>Department of Neuroscience, Physiology & Pharmacology, University College London, Gower Street,  
8 LONDON, WC1E 6BT, UK

9

10 <sup>b</sup>Science for Life Laboratory, School of Computer Science and Communication, KTH Royal Institute of  
11 Technology, Stockholm, Sweden

12

13 <sup>c</sup>Department of Neuroscience, Karolinska Institute, Solna, Sweden

14

15 <sup>1</sup>Correspondence: [m.gold@ucl.ac.uk](mailto:m.gold@ucl.ac.uk)

16

17

18

## 19 **Abstract**

20

21 Interplay between the second messengers cAMP and Ca<sup>2+</sup> is a hallmark of dynamic cellular processes. A  
22 common motif is the opposition of the Ca<sup>2+</sup>-sensitive phosphatase calcineurin and the major cAMP receptor,  
23 protein kinase A (PKA). Calcineurin dephosphorylates sites primed by PKA to bring about changes  
24 including synaptic long-term depression (LTD). AKAP79 supports signaling of this type by anchoring PKA  
25 and calcineurin in tandem. In this study, we discovered that AKAP79 increases the rate of calcineurin  
26 dephosphorylation of type II PKA regulatory subunits by an order of magnitude. Fluorescent PKA activity  
27 reporter assays, supported by kinetic modeling, show how AKAP79-enhanced calcineurin activity enables  
28 suppression of PKA without altering cAMP levels by increasing PKA catalytic subunit capture rate.  
29 Experiments with hippocampal neurons indicate that this mechanism contributes towards LTD. This non-  
30 canonical mode of PKA regulation may underlie many other cellular processes.

31

32

33

## 34 **Introduction**

35

36 Cyclic adenosine monophosphate (cAMP) and  $\text{Ca}^{2+}$  are ancient second messengers that are fundamental to  
37 the regulation of many dynamic cellular processes including synaptic plasticity (Huang et al., 1994), heart  
38 contraction (Bers et al., 2019), and glycogen metabolism (Roach et al., 2012). Crosstalk between the two  
39 second messengers is a common feature of cellular signaling. For example, cAMP can enhance cytosolic  
40  $\text{Ca}^{2+}$  entry by triggering phosphorylation of key ion channels (Qian et al., 2017; Schmitt et al., 2003) by its  
41 major intracellular receptor cAMP-dependent protein kinase, also known as Protein Kinase A (PKA).  
42 Similarly,  $\text{Ca}^{2+}$  can regulate cAMP levels by altering activities of both phosphodiesterases (Baillie et al.,  
43 2019) and adenylyl cyclases (Qi et al., 2019). At the receptor level, a common signaling motif is the  
44 opposition of PKA and the highly-abundant  $\text{Ca}^{2+}$ -sensitive phosphatase calcineurin (CN), with CN  
45 triggering cellular changes by removing phosphate from substrates primed by PKA. Notable examples of  
46 this motif are the regulation of postsynaptic substrates including AMPA-type glutamate receptors in the  
47 induction of long-term depression (LTD) of synaptic strength (Bear, 2003), and control of NFAT nuclear  
48 localization in immune responses (Hogan, 2017). According to current consensus, in these cases CN  
49 dephosphorylates substrates without any requirement for directly altering PKA activity (Dittmer et al.,  
50 2014; Lu et al., 2011; Tunquist et al., 2008; Weisenhaus et al., 2010; Zhang & Shapiro, 2016). This implies  
51 that energetically-costly futile cycles of phosphate addition and removal by PKA and CN must persist to  
52 maintain dephosphorylated substrate. It would be more logical for PKA activity to be switched off when  
53 CN is activated during substrate dephosphorylation. Uncovering the mechanism to achieve this is the focus  
54 of this study.

55

56 Recent years have seen renewed interest in mechanisms for regulating the release and re-capture of PKA  
57 catalytic subunits (Bock et al., 2020; Gold, 2019; Zhang et al., 2020), including new data that hint at how  
58 CN might directly suppress PKA activity. PKA is comprised of regulatory subunit dimers that bind and  
59 sequester PKA catalytic (C) subunits in an inhibited state (Taylor et al., 2019). PKA regulatory subunits  
60 are classified into type I subunits ( $\text{RI}\alpha$  and  $\text{RI}\beta$ ) that are predominantly cytosolic, and type II subunits ( $\text{RII}\alpha$   
61 and  $\text{RII}\beta$ ) that co-sediment with membranes (Gold, 2019). The regulatory subunit inhibitor sequence (IS)  
62 is phosphorylated upon association with C subunits for RII but not RI subunits, which bear alanine in place  
63 of serine in the phospho-acceptor site (S98 in  $\text{RII}\alpha$ ). Quantitative immunoblotting and mass spectrometry  
64 (MS) have recently shown that PKA regulatory subunits – and particularly RII subunits – greatly outnumber  
65 PKA C subunits (Aye et al., 2010; Walker-Gray et al., 2017) throughout the body. In addition, Zhang and  
66 co-workers (Zhang et al., 2015) have extended earlier observations (Rangel-Aldao & Rosen, 1976) to  
67 quantify differences in the rate of C subunit binding to RII subunits either phosphorylated (pRII) or

68 dephosphorylated at the IS. Remarkably, the  $k_{on}$  rate for C subunit association is ~50 times faster for  
69 dephosphorylated RII than pRII (Zhang et al., 2015) (**Figure 1A**). In theory, rapid dephosphorylation of  
70 RII subunits by CN could directly suppress PKA activity by increasing the rate of C subunit capture thereby  
71 reducing the proportion of C subunits that are dissociated (Buxbaum & Dudai, 1989; Isensee et al., 2018).  
72 While recent observations concerning PKA subunit stoichiometry and pRII/RII binding kinetics support  
73 this notion, isolated pRII is a low affinity substrate for CN with a half-maximal substrate concentration  
74 ( $K_m$ ) above 20  $\mu$ M (Perrino et al., 1992; Stemmer & Klee, 1994). Therefore, pRII dephosphorylation by  
75 CN would not be expected to occur to a meaningful degree at physiological concentrations in the absence  
76 of an additional factor.

77  
78 Anchoring proteins support signal transduction by elevating effective local concentrations of signaling  
79 proteins. A-kinase anchoring protein 79 (AKAP79; rodent ortholog AKAP150, gene name AKAP5) is a  
80 prototypical mammalian anchoring protein with several features that indicate it could operate in part by  
81 increasing the effective protein concentration of pRII subunits for CN. AKAP79 can simultaneously anchor  
82 both CN and PKA (Coghlan et al., 1995). It contains an amphipathic anchoring helix (Gold et al., 2006;  
83 Kinderman et al., 2006) for binding RII subunits, and a short linear ‘PIAIIIIT’ CN anchoring motif  
84 (Dell'Acqua et al., 2002; Li et al., 2012). The two anchoring sites are separated by only ~50 amino acids in  
85 the primary sequence within the C-terminus of AKAP79 (**Figure 1B**). AKAP79 is localized in dendritic  
86 spines where it is required for anchoring RII subunits (Tunquist et al., 2008). The anchoring protein is  
87 necessary for both induction of long-term depression (LTD) of CA3-CA1 hippocampal synapses (Lu et al.,  
88 2008; Tunquist et al., 2008; Weisenhaus et al., 2010), and for CN-mediated dephosphorylation of NFAT  
89 (Kar et al., 2014; Murphy et al., 2014) – both processes that are driven by CN dephosphorylation of sites  
90 primed by PKA. Despite these characteristics, the possibility that AKAP79 could support pRII  
91 dephosphorylation by CN has been disregarded perhaps because paradoxically AKAP79 acts as a weak  
92 inhibitor for CN dephosphorylation of 20-mer peptides corresponding to the phosphorylated RII IS  
93 (Coghlan et al., 1995; Kashishian et al., 1998). We reasoned that these assays could be misleading since  
94 peptide substrates are not subject to anchoring alongside CN that occurs for full-length RII subunits. To  
95 resolve this issue, in this study we measured how AKAP79 alters CN activity towards full-length pRII  
96 subunits. We went on to determine if AKAP79 can reduce the fraction of dissociated C subunits in concert  
97 with CN using fluorescence-based assays supported by kinetic modeling, before substantiating our  
98 observations in hippocampal neurons.

99  
100

## 101 Results

102

### 103 AKAP79 enables CN to efficiently dephosphorylate RII subunits at physiological concentrations

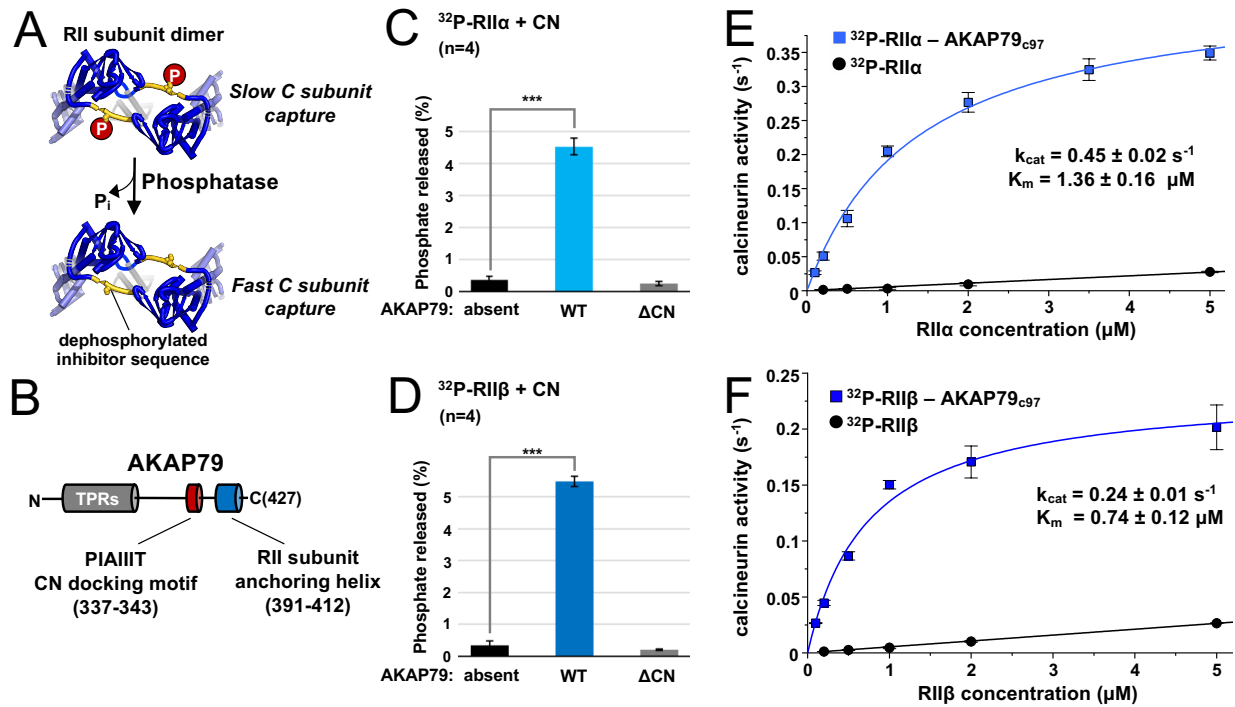
104 We set out to determine whether AKAP79 can increase CN dephosphorylation of full-length RII subunits  
105 phosphorylated at the IS. Using purified proteins (*Figure 1-figure supplement 1*), we compared  $^{32}\text{P}$  release  
106 from either pRII $\alpha$  (*Figure 1C*) or pRII $\beta$  (*Figure 1D*). Thirty second reactions were initiated by addition of  
107 excess  $\text{Ca}^{2+}$ /calmodulin (CaM) to 10 nM CN and 400 nM pRII subunits. For pRII $\alpha$  without AKAP79,  
108 phosphate was released from only  $0.36\pm 0.13$  % of the subunits (black, *Figure 1C*). Inclusion of full-length  
109 AKAP79 in the reaction mix increased phosphate release by 12.4-fold ( $p = 7.4\times 10^{-6}$ ) to  $4.52\pm 0.26$  % pRII $\alpha$   
110 subunits (light blue, *Figure 1C*). Removing the PIAIIIIT anchoring sequence in AKAP79 ( $\Delta\text{CN}$ ) returned  
111 dephosphorylation to a baseline level of  $0.26\pm 0.06$  % (grey, *Figure 1C*), consistent with a mechanism in  
112 which anchoring of CN adjacent to pRII subunits enhances the rate of dephosphorylation. Similar results  
113 were obtained for pRII $\beta$ , with addition of AKAP79 increasing phosphate release 16.3-fold ( $p = 3.0\times 10^{-6}$ )  
114 from  $0.34\pm 0.13$  % (black, *Figure 1D*) to  $5.49\pm 0.17$  % (dark blue, *Figure 1D*). Ablating the CN anchoring  
115 site in AKAP79 also reduced phosphorylation to a baseline level of  $0.2\pm 0.02$  % for this isoform (grey,  
116 *Figure 1D*).

117

118 We next measured CN phosphatase towards pRII over a range of pRII concentrations. We compared  
119 activity towards pRII subunits alone or in complex with a fragment of AKAP79 (AKAP79<sub>c97</sub>) encompassing  
120 positions 331-427 that includes the CN and RII subunit anchoring sites. Working with this stable highly-  
121 expressed construct enabled us to purify sufficient quantities of pRII $\alpha$ -AKAP79<sub>c97</sub> and pRII $\beta$ -AKAP79<sub>c97</sub>  
122 complexes (*Figure 1-figure supplement 1C & D*) to sample concentrations up to 5  $\mu\text{M}$ . In complex with  
123 AKAP79<sub>c97</sub>, both pRII $\alpha$  and pRII $\beta$  acted as relatively high affinity substrates of CN. pRII $\alpha$ -AKAP79<sub>c97</sub>  
124 (light blue, *Figure 1E*) was dephosphorylated with a half-maximal concentration ( $K_m$ ) of  $1.36\pm 0.16$   $\mu\text{M}$   
125 and turnover number ( $k_{\text{cat}}$ ) of  $0.45\pm 0.02$   $\text{s}^{-1}$ , and pRII $\beta$ -AKAP79<sub>c97</sub> with  $K_m = 0.74\pm 0.12$   $\mu\text{M}$  and  $k_{\text{cat}} =$   
126  $0.24\pm 0.01$   $\text{s}^{-1}$ . As expected, in the absence of the anchoring protein, pRII $\alpha$  and pRII $\beta$  subunits served as low  
127 affinity substrates for CN (black lines, *Figure 1E & F*). For both isolated pRII isoforms, the relationship  
128 between phosphatase activity and pRII concentration was linear up to 20  $\mu\text{M}$  (*Figure 1-figure supplement*  
129 *2*) – the highest concentration tested – indicative of a  $K_m$  of greater than 20  $\mu\text{M}$ . CN activity was very low  
130 ( $< 0.03$   $\text{s}^{-1}$ ) at concentrations of 5  $\mu\text{M}$  pRII or lower. This is consistent with earlier studies that reported a  
131  $K_m$  of 94  $\mu\text{M}$  for CN dephosphorylation of a phosphorylated 19-mer peptide derived from the RII $\alpha$  IS  
132 (Stemmer & Klee, 1994).

133





134

135

136

137

138

139

140

141

142

143

144

145

146

147

148

149

150

151

152

153

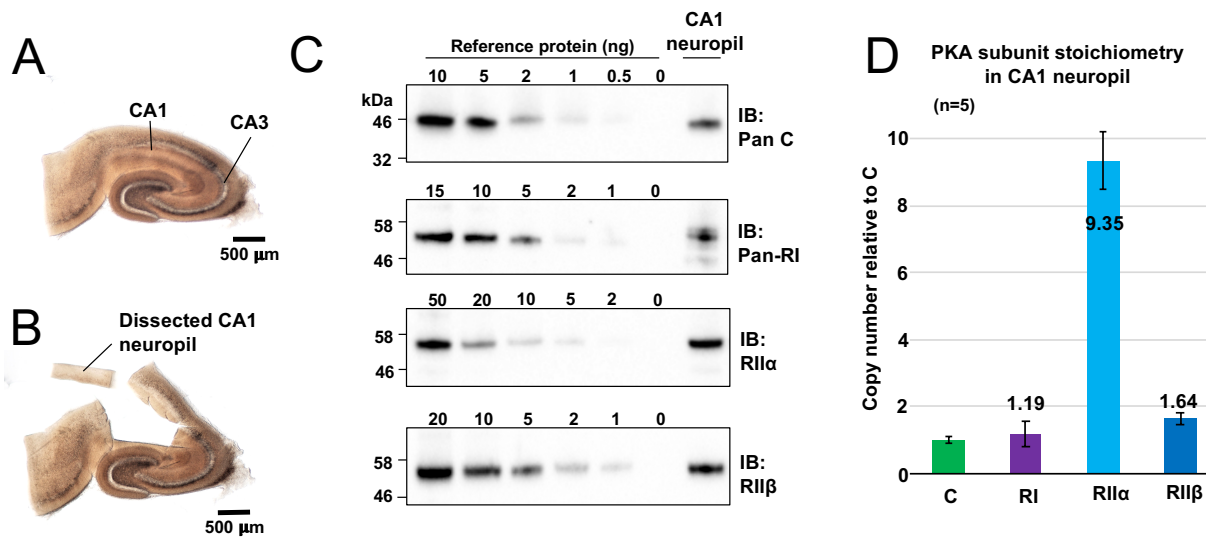
154

155

**Figure 1. Effect of AKAP79 on pRII dephosphorylation by CN.** (A) Dephosphorylation of the inhibitor sequence (IS, yellow) of RII subunits enables faster PKA C subunit capture. (B) AKAP79 contains anchoring sites for CN (red) and PKA RII subunits (blue) in its C-terminal region. Other macromolecular interactions are mediated through elements within its tandem polybasic regions (TPRs, grey). (C) CN-catalyzed phosphate release from pRII $\alpha$  subunits with either no AKAP79, WT AKAP79 (light blue), or AKAP79 lacking the PIAIIIIT anchoring motif ( $\Delta\text{CN}$ ). (D) CN-catalyzed phosphate release from pRII $\beta$  subunits with either no AKAP79, WT AKAP79 (dark blue), or AKAP79  $\Delta\text{CN}$ . (E) The relationship between CN activity towards pRII $\alpha$  subunits and pRII $\alpha$  concentration with pRII $\alpha$  subunits included either alone (black circles) or in complex with AKAP79<sub>c97</sub> (light blue squares). (F) The relationship between CN activity towards pRII $\beta$  subunits and pRII $\beta$  concentration with pRII $\beta$  subunits included either alone (black circles) or in complex with AKAP79<sub>c97</sub> (dark blue squares). For panels E & F, activities at each concentration were measured in triplicate. Statistical comparisons were performed using two-tailed unpaired Student *t*-tests. \*\*\**p* < 0.001.

To put our kinetic parameters for pRII dephosphorylation into a physiological context, we set out to determine accurate protein concentrations for PKA subunits in the CA1 neuropil where Schaffer collaterals from the CA3 region synapse onto CA1 dendrites (**Figure 2A**). These synapses are a leading prototype for understanding forms of LTD driven by CN following PKA priming (Bear, 2003). We collected hippocampal slices from 18-day old male Sprague-Dawley rats before micro-dissecting CA1 neuropil sections (**Figure 2B**). Following homogenization, concentrations of C, RII $\alpha$ , RII $\beta$ , and RI subunits in the extracted protein were determined using quantitative immunoblotting by running extracts (n=5) alongside

156 reference concentrations of purified PKA subunits (**Figure 2C**, **Figure 2-figure supplement 1**) (Walker-  
157 Gray et al., 2017). We found that RII $\alpha$  was by far the most predominant PKA subunit in the CA1 neuropil,  
158 accounting for  $0.32 \pm 0.029$  % total protein content compared to  $0.032 \pm 0.003$  % for C subunits,  $0.041 \pm 0.014$   
159 % for RI, and  $0.06 \pm 0.006$  % for RII $\beta$ . These numbers equate to a 9.4-fold higher molar abundance of RII $\alpha$   
160 subunits (light blue, **Figure 2D**) relative to C subunits with RI and RII $\beta$  present at similar levels to C  
161 subunits. The predominance of the RII $\alpha$  subunit is consistent with a previous imaging study of rodent  
162 hippocampus (Weisenhaus et al., 2010). Assuming that protein accounts for 8 % of total rat brain weight  
163 (Clouet & Gaitonde, 1956), we estimated RII subunit concentrations of 5.9  $\mu$ M (RII $\alpha$ ) and 1.03  $\mu$ M (RII $\beta$ ).  
164 These values fall within the range where CN efficiently dephosphorylates pRII only in the presence of  
165 AKAP79 (**Figure 1E & F**). Taken together our data therefore indicate that AKAP79 greatly enhances CN  
166 activity towards phosphorylated RII subunits at physiological concentrations.  
167

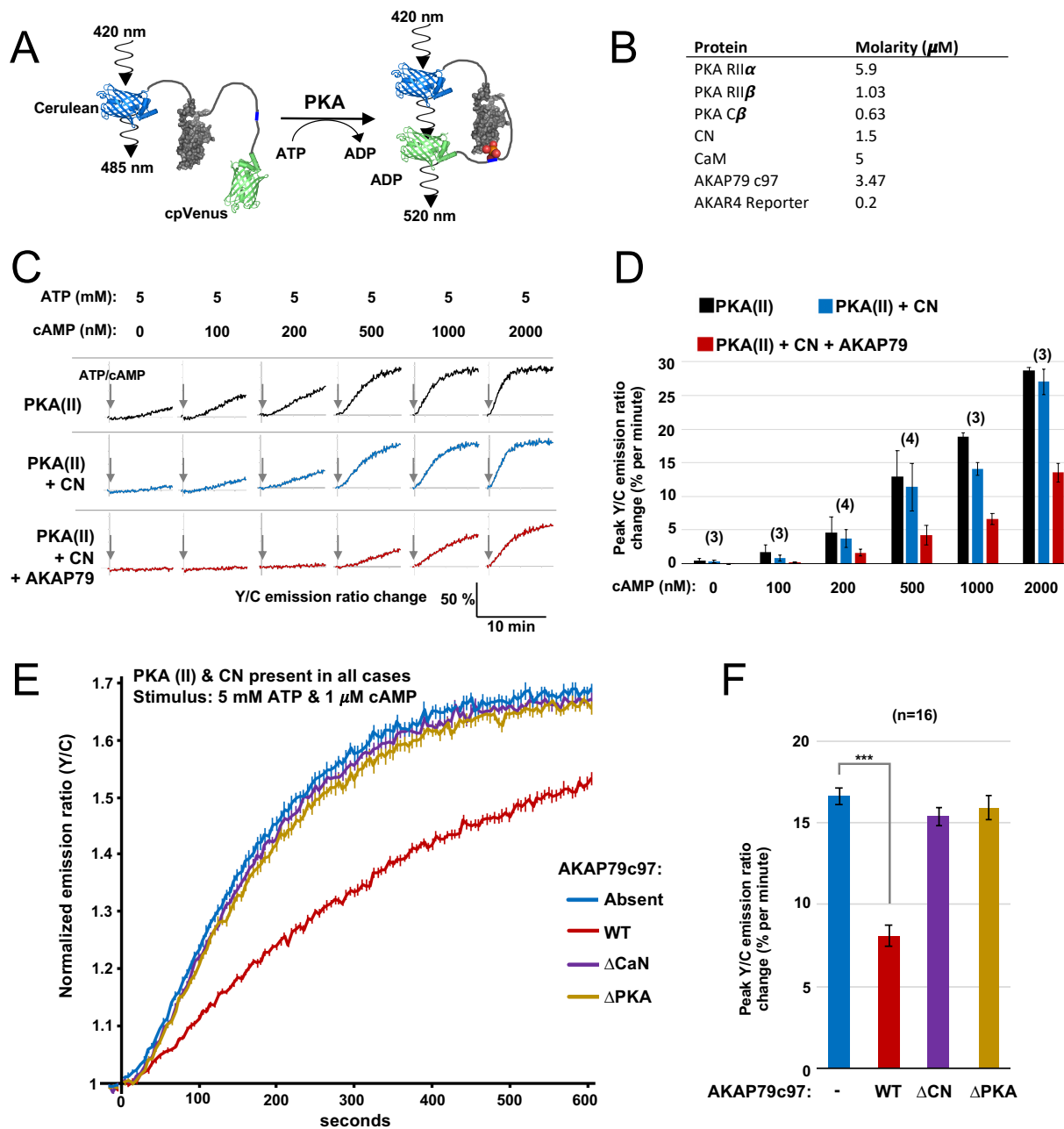


168  
169 **Figure 2. Quantitation of PKA subunits in CA1 neuropil.** Images of a P17 rat hippocampal slice before (A)  
170 and after (B) micro-dissection of the CA1 neuropil layer. (C) Immunoblots of CA1 neuropil extract for PKA  
171 subunits. Extracts were run alongside reference amounts of the relevant purified PKA subunit in each  
172 immunoblot (**Figure 2-figure supplement 1**). In each case, 15  $\mu$ g total protein extract was run alongside the  
173 reference series, with the exception of the anti-C immunoblot (10  $\mu$ g extract). (D) Copy numbers of PKA  
174 subunits in rat CA1 neuropil normalized to C subunits.  
175  
176

### 177 **AKAP79 enables calcineurin to suppress type II PKA activity**

178 Given that AKAP79 supports rapid pRII dephosphorylation by CN, we hypothesized that the AKAP could  
179 enable CN to directly reduce the fraction of dissociated C subunits in mixtures of RII and C subunits. To  
180 test this hypothesis, we utilized purified A-kinase activity reporter 4 (AKAR4) (**Figure 3A**). PKA

181 phosphorylation at threonine within the reporter's central 'LRRATTLVD' motif leads to a conformational  
182 change that increases FRET efficiency between the terminal fluorescent proteins (**Figure 3A**)(Depry et al.,  
183 2011). All AKAR4 experiments were performed using purified protein mixtures in 96-well plates. For each  
184 recording, three baseline 520/485 nm emission ratios were measured prior to injection of ATP and the  
185 desired concentration of cAMP into the protein mixture to initiate phosphorylation. Emission ratios were  
186 collected once every 5 seconds (s) thereafter. In calibration experiments with AKAR4 and different  
187 concentrations of C subunit only (**Figure 3-figure supplement 1A**), we found that the initial rate of AKAR4  
188 phosphorylation had a close to linear relationship to C subunit concentration up to 400 nM C subunit  
189 (**Figure 3-figure supplement 1B**). Full AKAR4 phosphorylation increased the emission ratio by 72 %  
190 (**Figure 3-figure supplement 1A**), consistent with previous studies (Depry et al., 2011). Importantly,  
191 supplementing these reactions with 1.5  $\mu$ M activated CN had no effect on AKAR4 phosphorylation rates,  
192 indicating that the phosphatase cannot directly dephosphorylate the reporter (**Figure 3-figure supplement**  
193 **1C & D**).



194

195 **Figure 3. FRET-based PKA activity measurements.** (A) AKAR4 mechanism: phosphorylation of the sensor

196 by PKA is detected as an increase in FRET between the terminal fluorescent proteins. (B) Concentrations of

197 proteins used for *in vitro* AKAR4 assays. Different experiments utilized different mixtures of these proteins

198 but always at these concentrations. (C) Representative AKAR4 traces showing change in 520 nm / 485 nm

199 (Y/C) emission ratio over time after injection of different concentrations of cAMP in tandem with 5 mM ATP.

200 All protein mixtures included AKAR4, type II PKA (RII $\alpha$ , RII $\beta$ , C), and CaM. Experiments were performed

201 with either no further additives (top row, black), with CN added (middle row, blue), or with both CN and

202 AKAP79<sub>c97</sub> added (bottom row, red). ATP/cAMP injections are indicated by arrows. (D) The chart shows peak

203 rates of emission ratio change for the recordings shown in the preceding panel. n values are stated above the

204 columns. (E) For these recordings, type II PKA, CN, and CaM were included in all cases. Phosphorylation was

205 initiated by injection of 5 mM ATP and 1  $\mu$ M cAMP at  $t=0$ . Averaged responses  $\pm$  standard error (SE) are  
206 shown with no further additives (blue), or when either WT (red),  $\Delta$ CN (purple), or  $\Delta$ PKA (gold) variants of  
207 AKAP79<sub>e97</sub> were included. (F) Peak rates (calculated between 30-90 s) for the responses shown in the  
208 preceding panel. Statistical comparisons were performed using two-tailed unpaired Student *t*-tests.  
209 \*\*\* $p < 0.001$ .

210

211

212 Next, we assembled purified protein mixtures with the aim of mimicking signaling involving PKA, CN,  
213 and AKAP79 in CA1 dendritic spines. RII $\alpha$ , RII $\beta$ , and C subunits were included at concentrations  
214 determined in CA1 neuropil extracts (**Figure 2**). CaM was added at a molar excess of 5  $\mu$ M, CN at 1.5  $\mu$ M  
215 (Goto et al., 1986), and AKAP79<sub>e97</sub> – when included – at half the concentration of total RII subunits  
216 (summarized in **Figure 3B**). RI subunits were omitted since they are not thought to be present in dendritic  
217 spines (Ilouz et al., 2017; Tunquist et al., 2008), and because the RI inhibitor site is not phosphorylated so  
218 cannot be regulated by CN. We first monitored AKAR4 phosphorylation in reactions containing RII $\alpha$ , RII $\beta$ ,  
219 C, and CaM (black, **Figure 3C**). Increasing the concentration of cAMP injected alongside ATP raised rates  
220 of AKAR4 phosphorylation as expected (black bars, **Figure 3D**). Supplementing the reactions with CN led  
221 to small but consistent decreases in the rate of AKAR4 phosphorylation at all cAMP concentrations (blue,  
222 **Figure 3C & D**). Rates were determined between 30-90 s in the linear early phase that followed a brief ~15  
223 second delay, with the exception of the lowest two cAMP concentrations (0 & 100 nM), where relatively  
224 slow rates were calculated between 30-330 s. Additional supplementation with AKAP79<sub>e97</sub> markedly  
225 decreased the rate of AKAR4 phosphorylation (red, **Figure 3C**). For example, with 1  $\mu$ M cAMP activation,  
226 addition of both CN and the AKAP reduced the initial rate of AKAR4 phosphorylation by 2.8-fold from  
227 18.9 $\pm$ 0.6 to 6.7 $\pm$ 0.8 % per minute ( $p = 0.0007$ , black and red bars, **Figure 3D**). To confirm that AKAP79  
228 enables CN to suppress PKA activity by anchoring it alongside RII subunits, we investigated the effect of  
229 removing either the CN (positions 337-343) or PKA (391-400) anchoring sites. At 1  $\mu$ M cAMP activation,  
230 addition of wild-type (WT) AKAP79<sub>e97</sub> (red, **Figure 3E & F**) reduced the initial rate of AKAR4  
231 phosphorylation by 2.06-fold ( $p = 2.7 \times 10^{-11}$ ) compared to supplementation with only CN (blue). Similar  
232 AKAR4 responses were obtained when either the AKAP was omitted altogether (blue, **Figure 3E & F**), or  
233 if either the CN (purple) or PKA (orange) anchoring sites in the AKAP were removed. Overall, these  
234 AKAR4 measurements reveal that AKAP79 enables CN to robustly decrease type II PKA activity by  
235 anchoring the two enzymes together.

236

### 237 **Mechanistic basis of PKA suppression by calcineurin and AKAP79**

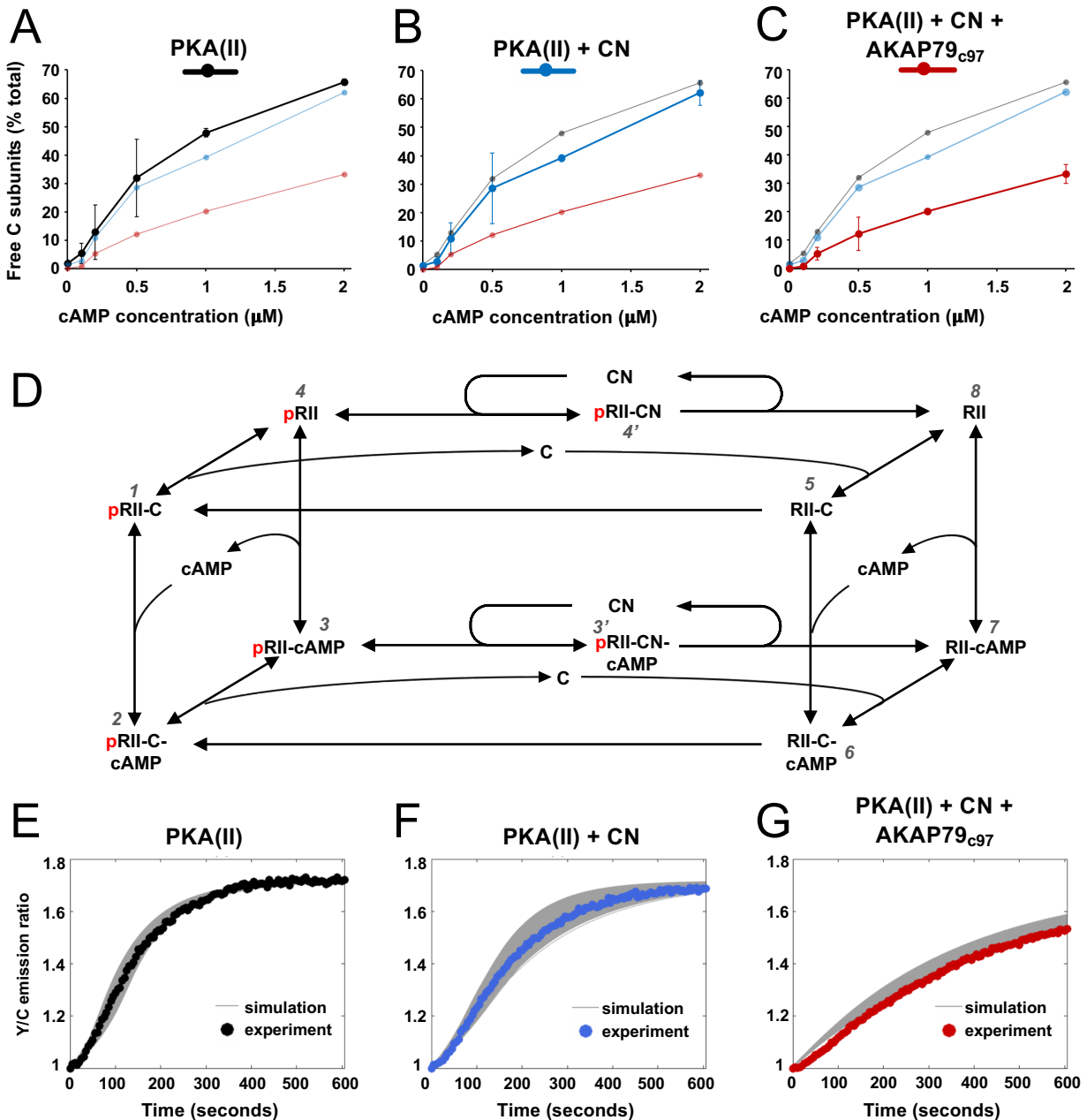
238 We next aimed to quantify how AKAP79 and CN changed the fraction of free C subunits in our reaction  
239 mixtures. To estimate this, we cross-referenced rates of AKAR4 phosphorylation recorded in the ‘spine

240 mimic' reaction mixtures (**Figure 3C & E**) to the reference curve ( $r = 0.998$ ) obtained with only C subunits  
241 (**Figure 3-figure supplement 1B**). We focused on determining free C subunit concentrations during the  
242 early period of linear change (30-90 s for cAMP concentrations of 0.2  $\mu\text{M}$  and above) where we assume  
243 the underlying kinetics are close to equilibrium. We calculated free C subunit concentrations following this  
244 approach using all available data between 0 to 2  $\mu\text{M}$  cAMP (**Figure 3-figure supplement 1E**). The  
245 calculated proportion of C subunits that are dissociated at different cAMP concentrations are shown for  
246 type II PKA + CaM either alone (black, **Figure 4A**), with CN (blue, **Figure 4B**), or with both CN and  
247 AKAP79<sub>c97</sub> (red, **Figure 4C**). Together, AKAP79 and CN reduced the proportion of free C subunits at  
248 equilibrium across the cAMP concentration range including from  $47.8 \pm 1.5$  to  $20.2 \pm 0.8$  % at 1  $\mu\text{M}$  cAMP,  
249 and from  $65.7 \pm 1.1$  to  $33.2 \pm 3.3$  % at 2  $\mu\text{M}$  cAMP (**Figure 4A & C**). The effect of adding CN alone was  
250 limited (**Figure 4B**), consistent with the much lower activity of the phosphatase towards pRII subunits in  
251 the low micromolar range (**Figure 1E & F**).

252  
253 To understand at a deeper level how CN and AKAP79 reduce the fraction of free C subunits, we updated  
254 and extended a kinetic model (Buxbaum & Dudai, 1989) that takes into account transitions between pRII  
255 (left-hand square, **Figure 4D**) and unphosphorylated RII subunits (right-hand square). The extended model  
256 also incorporates AKAR4 binding to and phosphorylation by free C subunits. We used a Bayesian approach  
257 (Eriksson et al., 2019) to estimate parameter sets for the model that could fit data pooled from AKAR4  
258 recordings obtained after stimulation with 1 and 2  $\mu\text{M}$  cAMP (**Figure 3C & E**). A log uniform prior  
259 parameter distribution was used as a starting point for the Bayesian method, with the bounds of each  
260 parameter set according to empirical data (**Supplementary Table 1**), including rates of pRII  
261 dephosphorylation determined in this study (**Figure 1**), and binding rates of C subunits to pRII and RII  
262 (Zhang et al., 2015). This approach was terminated after identifying approximately 10,000 parameter sets  
263 that could explain the experimental data (**Figure 4E-G**). Simulations using these parameter sets capture the  
264 initial delay that occurs in the first  $\sim 15$  s since all reactions initially start with dephosphorylated RII  
265 subunits (e.g., grey lines, **Figure 4E**), and they enabled us to predict concentration changes of individual  
266 states within the model that cannot be determined experimentally (first three columns, **Figure 4-figure**  
267 **supplement 1**). The model indicates that AKAP79 and CN together shift C subunit capture to the faster  
268 right-hand square sub-system (**Figure 4D**), driving down the fraction of free C subunits and thereby  
269 reducing PKA activity.

270





271

272

273

274

275

276

277

278

279

280

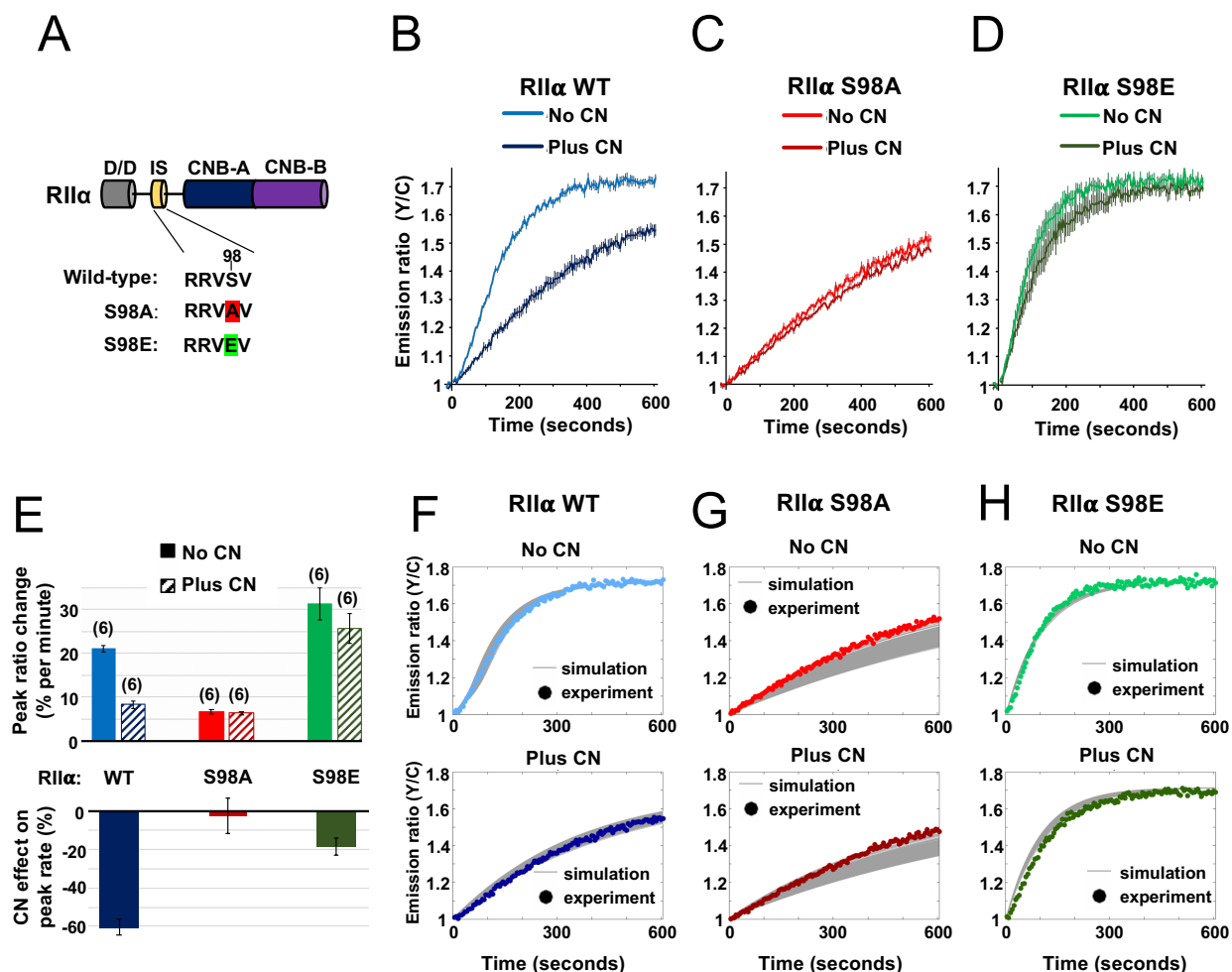
281

**Figure 4. Kinetic analysis of PKA-CN-AKAP79 signaling.** (A-C) Estimates of the average proportion of free C subunits between 30-90 s for type II PKA alone (black), with CN (blue), and with both CN and AKAP79<sub>c97</sub> (red) following activation of the protein mixtures with a range of cAMP concentrations. (D) Reaction scheme used for modeling type II PKA regulation by CN. Each species within the scheme is numbered consistent with supporting data in figure in *Supplementary Table 1*. (E-G) Model simulations for protein mixtures activated with 1  $\mu$ M cAMP are shown with the experimental data overlaid. Averaged values are shown for experimental data after pooling the data shown in *Figure 3*. Responses are shown for type II PKA alone (E), with CN (F), and with both CN and AKAP79<sub>c97</sub> (G). A sample of the corresponding simulated responses are shown in grey. An ‘error’ threshold of 0.01 was used to accept curves as a good fit.

282 **Mutation of the RII $\alpha$  IS phosphorylation site occludes PKA suppression by CN**

283 The results of the preceding sections show that AKAP79 targeting of CN for direct suppression of PKA is  
284 a viable mechanism for LTD induction. Previously published studies in hippocampal slices involving  
285 genetic manipulation of AKAP150 (the rodent ortholog of AKAP79) are also consistent with this  
286 mechanism. Full AKAP150 knock-out (Lu et al., 2008; Tunquist et al., 2008; Weisenhaus et al., 2010), or  
287 AKAP150 knock-in with variants lacking either the PKA or CN anchoring sites (Jurado et al., 2010;  
288 Sanderson et al., 2016), show that both AKAP150 anchoring sites are required for LTD induction. However,  
289 such approaches cannot distinguish between CN targeting to pRII subunits versus other substrates. If direct  
290 suppression of PKA activity by CN is essential for LTD induction, we reasoned that mutation of the IS  
291 phospho-acceptor S98 (**Figure 5A**) in the predominant RII $\alpha$  isoform would be expected to disrupt LTD  
292 induction in CA1 neurons. To confirm this presupposition before undertaking experiments in neurons, we  
293 re-ran AKAR4 experiments at 1  $\mu$ M cAMP substituting in either S98A or S98E RII $\alpha$ . For each RII $\alpha$  variant  
294 (**Figure 1-figure supplement 1H**), we compared responses with or without CN, with WT RII $\beta$  and  
295 AKAP79<sub>c97</sub> present in all cases. For WT RII $\alpha$ , addition of CN to the mixture decreased the peak rate of  
296 AKAR4 phosphorylation from 21.02 $\pm$ 0.76 (light blue, **Figure 5B**) to 8.24 $\pm$ 0.79 % per minute (dark blue).  
297 Substituting in RII $\alpha$  S98A generated slow rates of AKAR4 phosphorylation in both cases (6.30 $\pm$ 0.44 % per  
298 min with CN, and 6.67 $\pm$ 0.56 % without, **Figure 5C**). Conversely, the peak rate of AKAR4 phosphorylation  
299 was high regardless of the presence of CN for the S98E RII $\alpha$  variant (31.30 $\pm$ 3.60 % per min without CN;  
300 25.65 $\pm$ 3.44 % with CN, **Figure 5D**). Together, this data indicates that substituting in either mutant of RII $\alpha$   
301 in neurons would be expected to reduce LTD induction in neurons if direct suppression of PKA by CN is  
302 required in LTD induction (**Figure 5E**).

303



304  
305  
306  
307  
308  
309  
310  
311  
312  
313  
314  
315  
316  
317  
318  
319  
320  
321

**Figure 5. Characterization of RII $\alpha$  IS phosphorylation site mutations.** (A) RII $\alpha$  subunit topology showing locations of the docking and dimerization domain (D/D, grey), inhibitor sequence (IS, yellow), and tandem cyclic nucleotide binding domains (dark and light blue). S98A (red) and S98E (green) mutations in the IS are highlighted. (B-D) Comparison of AKAR4 emission ratio changes following 5 mM ATP/1  $\mu$ M cAMP activation of protein mixtures containing either WT (B), S98A (C), or S98E (D) RII $\alpha$ . 1.03  $\mu$ M RII $\beta$  was included in all cases. Measurements were collected either with or without CN in the reaction mixture. Averaged responses ( $\pm$  SE) are shown for WT RII $\alpha$  with (dark blue) and without CN (light blue), S98A RII $\alpha$  with (dark red) and without (light red) CN, and RII $\alpha$  S98E with (dark green) and without (light green) CN. (E) The upper bar chart shows peak rates (calculated between 30-90 s) for the responses shown in panels b-d. The effect of including CN in the reaction mixture for each RII variant is shown in the lower bar chart. (F-H) Model predictions in the six conditions of panels b-d are shown in grey when simulating using the ‘extended’ model (see Methods) and using the different parameter sets generated from the parameter estimation approach. The same parameters as retrieved using data shown in figure 4 were used as a starting point for the simulations, but parameter sets were filtered based on data collected with RII $\alpha$  S98A. Model predictions are shown alongside the corresponding experimental data collected with either WT (F), S98A (G), or S98E (H) RII $\alpha$  in the reaction mix.

322

323 Before moving on to experiments in neurons, we used the data collected with RII $\alpha$  variants to test the  
324 accuracy of our kinetic modeling. We ran simulations assuming that the S98A and S98E variants of RII $\alpha$   
325 would behave like dephosphorylated and phosphorylated forms of the regulatory subunit. Broadly, the  
326 simulations were in line with our experimental data and predicted that addition of CN would reduce PKA  
327 activity substantially more in the WT but not RII $\alpha$  mutant conditions (**Figure 4-figure supplement 1**), with  
328 low and high PKA activities regardless of CN concentration for the S98A and S98E variants, respectively.  
329 The model predictions for the extent by which AKAR4 phosphorylation was depressed in the RII $\alpha$  S98A  
330 system were, however, spread out depending on the specific parameter set (column 4-5, **Figure 4-figure**  
331 **supplement 1**). This implies that the WT data we used to constrain the model were not sufficient to precisely  
332 constrain the dynamics specifically for the unphosphorylated RII sub-system (right square, **Figure 4D**) To  
333 understand the characteristics of those parameter sets that also reproduced the RII $\alpha$  S98A behavior, we  
334 filtered the parameter sets returned by the parameter estimation approach into two classes depending on  
335 whether they fit closely (blue, **Figure 4-figure supplement 1**) or not (red) to the acquired mutation data,  
336 yielding 422 parameter sets that fit closely to both the WT and mutation data. A pairwise coordinate plot  
337 (see **Figure 5-figure supplement 1A**) shows that, overall, the two classes of parameter sets do not appear  
338 to be visually distinct with regards to kinetic rates. However, analysis and subdivision of the eight model  
339 dissociation constants ( $K_D$ 's) reveals an interesting relation among them (**Figure 5-figure supplement 1B**).  
340 As shown by the scatterplots for the  $K_D$  for interaction between RII-C and cAMP ( $K_{D56}$ ) and RII-cAMP  
341 and C ( $K_{D76}$ ) (**Figure 5-figure supplement 1C**),  $K_{D56}$  should be relatively low within its range paired with  
342 a relatively high  $K_{D76}$  (**Figure 5-figure supplement 1D**) to accurately mimic the biological workings of  
343 the PKA sub-system. This pairing ensures that sufficient C subunit is released by cAMP when the kinetics  
344 are restrained to the unphosphorylated RII sub-system when the RII $\alpha$  S98A mutation is introduced. Overall,  
345 simulations using unfiltered (top row, **Figure 4-figure supplement 1**) and filtered (**Figure 5F-H**) parameter  
346 sets show that the kinetic model closely reproduces the experimental data, especially when further  
347 constrained using data collected with RII $\alpha$  S98A. Taken together, experiments and simulations with S98A  
348 and S98E variants of RII $\alpha$  show that either of these mutations should prevent AKAP79 and CN from  
349 switching C subunit capture from the left-hand square sub-system to the faster right-hand square (**Figure**  
350 **4D**). Therefore, either substitution would be expected to reduce LTD induction if the mechanism is  
351 important *in vivo*.

352

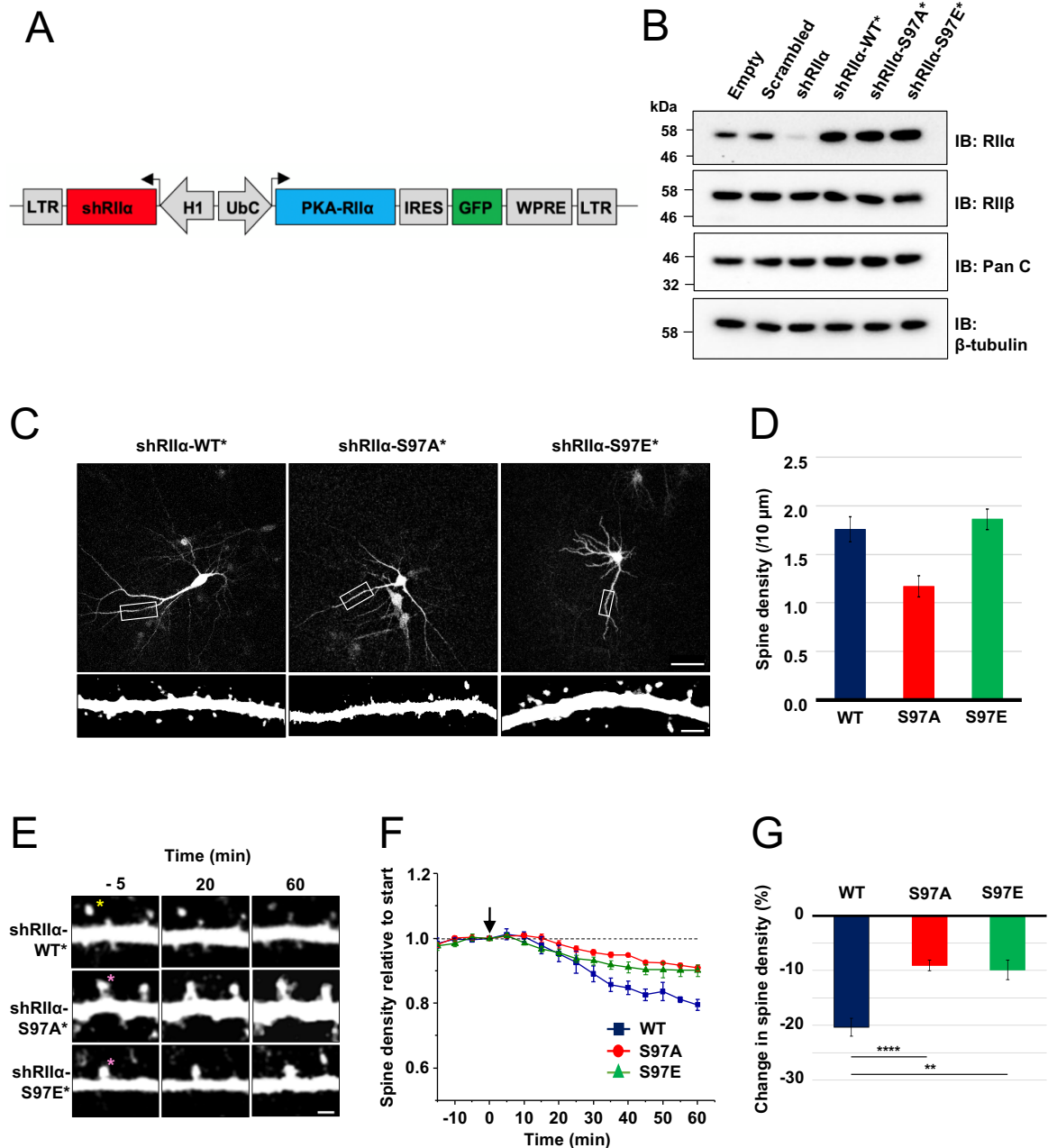
### 353 **Disruption of RII $\alpha$ phosphorylation in CA1 neurons impedes chemical LTD**

354 To enable neuronal RII $\alpha$  replacement experiments, we generated lentiviruses for shRNA-mediated  
355 knockdown of endogenous RII $\alpha$  and simultaneous expression of shRNA-resistant RII $\alpha$  variants in tandem

356 with GFP. The lentiviruses contain an H1 promoter for expression of a highly-effective shRNA targeted to  
357 RII $\alpha$  (**Figure 6A**). A UbC promoter drives expression of replacement RII $\alpha$  sequences in tandem with GFP,  
358 with an internal ribosome entry sequence (IRES2) between the coding sequences of the two proteins  
359 enabling expression of GFP. We validated the lentiviruses in dissociated rat primary hippocampal neurons  
360 by comparing the efficacy of five different lentiviruses. On day 7 *in vitro* (DIV7), we infected with control  
361 lentiviruses expressing either scrambled or shRII $\alpha$  RNA, or with complete viruses for replacement of  
362 endogenous RII $\alpha$  with either WT, S97A, or S97E (RII $\alpha$  in rat is equivalent to S98 in human RII $\alpha$ ). Neuronal  
363 protein extracts were collected on DIV14, and analyzed using immunoblotting. Anti-RII $\alpha$  immunoblotting  
364 (top row, **Figure 6B**) confirmed effective suppression of endogenous RII $\alpha$  with shRII $\alpha$  (lane 3) but not  
365 scrambled RNA (lane 2), and strong expression of the replacement sequences (lanes 4-6). Expression of  
366 PKA C (row 2, **Figure 6B**) and RII $\beta$  subunits (row 3) was not affected by lentiviral infection in any case.  
367 Blocking PKA activity with H89 is known to prevent growth of new spines, whereas stimulating PKA with  
368 forskolin increases spine formation (Kwon & Sabatini, 2011). Replacing RII $\alpha$  with the S97A variant –  
369 which has lower PKA activity regardless of CN activity (**Figure 5F**) – would therefore be expected to lead  
370 to a reduction in spines. To test this, we imaged dendritic spines on primary hippocampal neurons  
371 expressing either WT (left panel, **Figure 6C**), S97A (middle panel), or S97E (right panel) RII $\alpha$ . Consistent  
372 with a role for PKA in spinogenesis, spine density was reduced by 33.5 % ( $p=0.002$ ) in neurons expressing  
373 the S97A variant to  $1.17\pm 0.11$  spines per 10  $\mu\text{m}$  compared to  $1.76\pm 0.12$  for WT RII $\alpha$ . Spine density for the  
374 S97E variant was similar to WT at  $1.86\pm 0.11$  spines/10  $\mu\text{m}$ .

375  
376 To test whether the two substitutions at RII $\alpha$  S97 affect LTD, we monitored changes in dendritic spine  
377 number during chemical LTD – a model of long-term synaptic depression that can be applied in dissociated  
378 neuronal cultures. Bath application of 20  $\mu\text{M}$  NMDA for 3 minutes triggered a steady reduction in spine  
379 density (**Figure 6E**, top row) in neurons expressing WT RII $\alpha$  as expected (Zhou et al., 2004), reaching a  
380  $20.4\pm 1.6$  % reduction in spines after one hour (blue, **Figure 6F**). In comparison, spine loss was attenuated  
381 in neurons expressing either the S97A (**Figure 6E**, middle row) or S97E (bottom row) RII $\alpha$  variants. Spine  
382 numbers were reduced by only  $9.07\pm 0.96$  % in neurons expressing RII $\alpha$  S97A (red line, **Figure 6F**), and  
383 by  $9.90\pm 1.8$  % for the S97E variant (green line). The residual LTD in both conditions may correspond to  
384 action of CN on substrates other than pRII subunits, and limited suppression of PKA activity through CN  
385 dephosphorylation of the relatively small number of WT RII $\beta$  subunits that are present in all cases. Overall,  
386 attenuation of spine loss in neurons expressing either S97A ( $p=0.00046$ ) and S97E ( $p=0.0014$ ) RII $\alpha$   
387 compared to WT subunits is consistent with an important role for direct PKA activity suppression by CN  
388 during the induction of LTD.

389



390

391 **Figure 6. Lentivirus development and spine density imaging.** (A) Schematic of the FUGW-H1-based

392 lentiviral vector used to knock down and replace endogenous RII $\alpha$  subunits in dissociated hippocampal

393 cultures. (B) To validate lentiviruses, dissociated hippocampal neurons were infected on the seventh day *in*

394 *vitro* (DIV7). Immunoblots are shown comparing neuronal extracts collected on DIV14 after infection with no

395 virus, virus expressing scrambled shRNA only, shRII $\alpha$  only, and the three complete lentiviruses for

396 knockdown/replacement with either WT, S97A, or S97E RII $\alpha$ . (C) Representative live-cell images of

397 lentivirus-infected primary hippocampal neurons at DIV14 expressing either WT, S97A, or S97E RII $\alpha$ . Scale

398 bars correspond to 50  $\mu$ m (upper panels) and 5  $\mu$ m (lower panels). (D) Average spine density on hippocampal

399 dendrites following lentiviral replacement of endogenous RII $\alpha$ . Data were averaged from 106 (WT), 97 (S97A),

400 and 113 (S97E) neurons derived from 7 rats for each condition, and are represented as mean  $\pm$  SE. Conditions



401 were compared using one-way ANOVA with Turkey post-hoc tests. (E) Representative live-cell images  
402 showing dendritic spines in primary hippocampal neurons expressing either WT, S97A, or S97E replacement  
403 RII $\alpha$  at three points before and after chem-LTD (scale bar = 2.5  $\mu$ m). Chem-LTD was induced at t=0 with 20  
404  $\mu$ M NMDA for 3 minutes. The yellow asterisk indicates a spine that disappeared over the course of the protocol  
405 whereas the pink asterisks indicate spines that did not. (F) Plot showing average changes in spine density ( $\pm$   
406 S.E) in primary hippocampal neurons expressing either WT (dark blue), S97A (red) or S97E (green) RII $\alpha$ . (G)  
407 Average changes in spine density  $\pm$  SE one hour after induction of chem-LTD are shown for neurons expressing  
408 WT (dark blue, n=5), S97A (red, n=5), and S97E (green, n=4) RII $\alpha$  variants as shown in the preceding two  
409 panels. Statistical comparisons were performed by 2-way ANOVA followed by Bonferroni's post-hoc test.  
410 \*\* $p$ <0.01, \*\*\* $P$ <0.001

411

412

## 413 Discussion

414

415 The observations in this study support a revised mechanism for CN-mediated long-term depression in CA1  
416 model synapses. AKAP79/150 is critical for anchoring PKA in dendritic spines (Tunquist et al., 2008;  
417 Weisenhaus et al., 2010) through association with RII subunits, which are the predominant neuronal PKA  
418 subunit in  $\sim$ 11-fold molar excess of C subunits in the CA1 neuropil (**Figure 2D**). Imaging studies (Ilouz et  
419 al., 2017; Weisenhaus et al., 2010) are consistent with our quantitative immunoblotting data, which show  
420 that RII $\alpha$  is the major RII isoform in the CA1 neuropil. pRII dephosphorylation is limited prior to Ca<sup>2+</sup>  
421 stimulation (**Figure 7A**), enabling a tonic level of dissociated C subunits sufficient to basally phosphorylate  
422 postsynaptic substrates in dendritic spines such as GluA1 subunits of AMPA-type glutamate  
423 receptors (Bear, 2003). LTD is brought about by CN (Mulkey et al., 1994), which is activated by Ca<sup>2+</sup>  
424 entering spines through NMDA-type glutamate receptors (**Figure 7B**). AKAP79/150 contains a 'PIAIIIIT'  
425 CN anchoring motif that is necessary for LTD (Jurado et al., 2010; Sanderson et al., 2012). In addition to  
426 potentially targeting CN to postsynaptic substrates including GluA1 subunits, the PIAIIIIT anchoring motif  
427 positions CN adjacent to pRII subunits where it can efficiently dephosphorylate them (**Figure 7B**). This  
428 enables CN to increase the concentration of dephosphorylated RII species (blue spheres in the kinetic  
429 scheme shown in **Figure 7B**) thereby directly suppressing PKA activity by increasing the rate of PKA C  
430 subunit capture. Consistent with this mechanism, blocking regulation of RII phosphorylation state by  
431 introducing mutations that mimic either the phosphorylated or dephosphorylated forms of the IS reduces  
432 LTD in cultured hippocampal neurons.

433

434 Our discovery that CN can directly suppress PKA activity in the AKAP79 complex reconciles three aspects  
435 of AKAP79 structure and function that had been enigmatic and paradoxical. First, previous studies showed  
436 that AKAP79 acts as a weak inhibitor of CN towards peptide substrates including a 20-mer peptide

437 encompassing the phosphorylated RII IS (Coghlan et al., 1995; Kashishian et al., 1998), apparently at odds  
438 with the functional requirement for the anchoring protein in targeting CN to bring about LTD. We show  
439 that the key substrate for CN is likely to be full-length pRII subunits, and that in fact AKAP79 enhances  
440 the activity towards pRII at physiological concentrations by more than ten-fold. A second enigmatic feature  
441 of AKAP79 is its CN anchoring motif, PIAIIT, which includes an additional central residue compared to  
442 the typical PxIxIT motif (Roy & Cyert, 2009). In a crystal structure of CN in complex with a peptide  
443 corresponding to AKAP79 positions 336-346, the additional leucine supports simultaneous binding of two  
444 copies of CN on either side of the motif (Li et al., 2012). Native mass spectrometry measurements of a  
445 purified AKAP79-CN-CaM-RII $\alpha$  D/D complex also support a stoichiometry of 2 CN to 1 AKAP79 (Gold  
446 et al., 2011), although solution measurements indicate that when full-length RII subunits are bound to  
447 AKAP79, only one copy of CN can bind at a time (Li et al., 2012; Nygren et al., 2017). One possible  
448 explanation for this behavior is that CN binds transiently to either side of the AKAP79 PIAIIT motif  
449 enabling it to access both protomers of RII anchored to AKAP79 for efficient pRII dephosphorylation  
450 (cartoon representations in **Figure 7**). This idea is consistent with data showing that mutating the PIAIIT  
451 motif to a high-affinity canonical PxIxIT motif impairs the function of the phosphatase (Li et al., 2012).  
452 Third, existing models of AKAP79 function assume that CN anchored to AKAP79 overcomes PKA  
453 phosphorylation at substrates with no reduction in PKA phosphorylation rate. In our revised mechanism,  
454 CN directly suppresses PKA activity when removing phosphate from substrates primed by PKA thereby  
455 avoiding energetically-costly ongoing futile cycling of phosphorylation and dephosphorylation by PKA and  
456 CN at these sites.  
457  
458

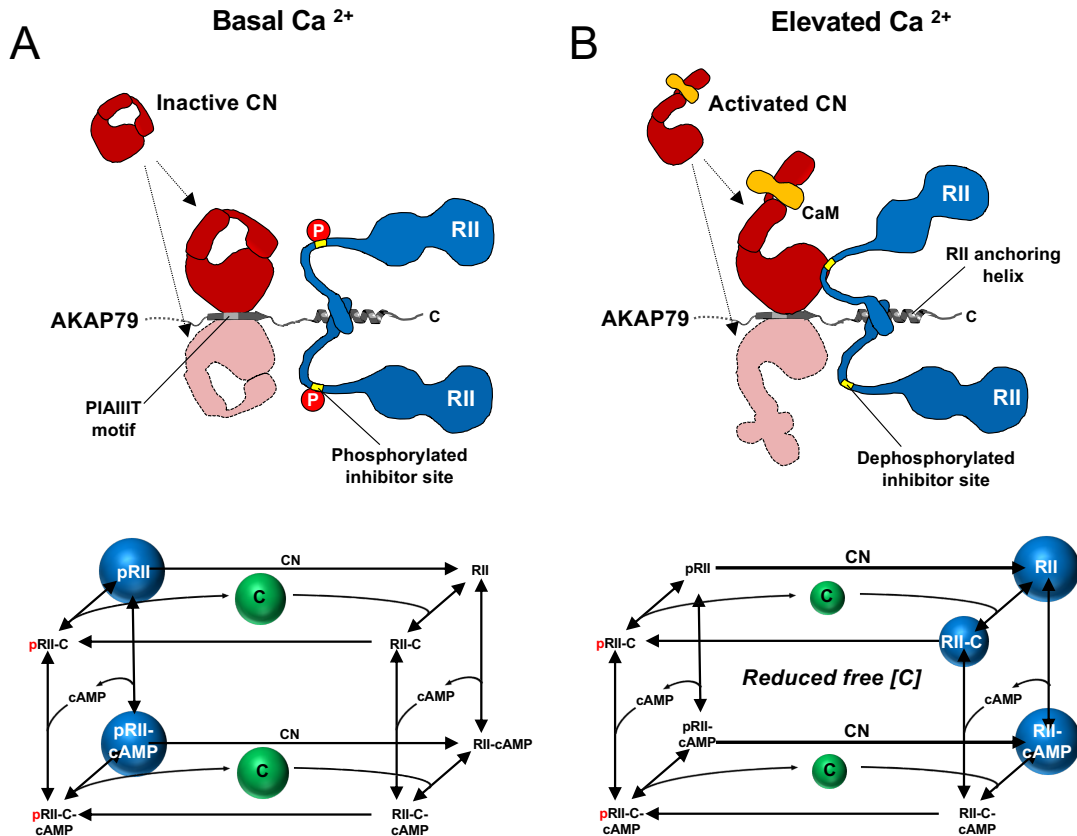


**Figure 7. Summary model of PKA suppression by CN within the AKAP79 complex.** Structural and kinetic models (upper and lower panels, respectively) of signaling within the AKAP79 complex are shown under conditions of either low (A) or elevated  $Ca^{2+}$  (B). Elevated  $Ca^{2+}$  triggers CN (red) dephosphorylation of pRII (blue) which shifts C subunit capture from the left-hand square of the kinetic scheme to the right-hand square which features dephosphorylated forms of RII. The overall effect is a reduction in the concentration of free C subunits. The most abundant forms of RII under the two conditions are highlighted by blue spheres.

468 A challenge in the future will be to understand how the mechanism uncovered here relates to the full  
 469 complexity of AKAP79 function. AKAP79 is directly regulated by  $Ca^{2+}$ /CaM, which binds to a 1-4-7-8  
 470 hydrophobic motif (Patel et al., 2017) starting at position W79. Binding of  $Ca^{2+}$ /CaM releases AKAP79  
 471 from the postsynaptic membrane (Dell'Acqua et al., 1998) and alters the conformation of the signaling  
 472 complex by triggering formation of a second interface between CN and AKAP79 that involves an LxVP-  
 473 type motif in AKAP79 (Gold et al., 2011; Nygren et al., 2017). It will be important to understand how this  
 474  $Ca^{2+}$ -sensitive interface affects CN suppression of PKA activity. Localization of AKAP79 is also regulated  
 475 by palmitoylation at C36 and C139 (Delint-Ramirez et al., 2011; Keith et al., 2012). Palmitoylation is  
 476 required for endosomal localization of AKAP79, and AKAP79 depalmitoylation and synaptic removal is  
 477 additionally regulated by CaMKII (Woolfrey et al., 2018). Our work suggests that removal of AKAP79

478 from synapses might be synchronized with accumulation of inhibited C subunits in the AKAP79 complex.  
479 AKAP79 is a highly multivalent protein – other notable documented interaction partners include protein  
480 kinase C (Hoshi et al., 2010) and the Ca<sup>2+</sup>-activated cyclase AC8 (Baldwin & Dessauer, 2018; Zhang et al.,  
481 2019). Oscillations of Ca<sup>2+</sup>, cAMP, and PKA activity have been observed in pancreatic  $\beta$ -cells (Hinke et  
482 al., 2012; Ni et al., 2011), and knockout of AKAP150 leads to the loss of cAMP oscillations in  $\beta$ -cells upon  
483 stimulation with insulin (Hinke et al., 2012). CN dephosphorylation of pRII subunits bound to AKAP79 is  
484 likely to play a role in oscillatory patterns of PKA activity, and it will be important to understand how this  
485 mechanism underlies responses to short-lived and oscillatory changes in Ca<sup>2+</sup> and cAMP concentration.

486

487 In this combined experimental-computational study, we focused on AKAP79 signaling in dendritic spines  
488 on the basis that this could serve as a prototype for understanding a potentially widespread non-canonical  
489 mechanism for altering PKA. In addition to its role in dendritic spines, AKAP79 regulates many different  
490 membrane channels and receptors following Ca<sup>2+</sup> influx through a variety of sources, and the mechanism  
491 that we have uncovered here is likely to at least extend to these additional contexts. For example, AKAP79  
492 underlies GABA<sub>A</sub> receptor regulation during LTD of GABAergic synapses (Dacher et al., 2013), and it  
493 positions PKA and CN for regulation of TRPV channels (Zhang et al., 2008), Kv7 channels (Zhang &  
494 Shapiro, 2012), and both  $\beta$ -adrenergic receptor isoform (Houslay & Baillie, 2005). AKAP79 is also  
495 necessary for NFAT dephosphorylation following Ca<sup>2+</sup> entry through both L-type calcium channels (Wild  
496 et al., 2019) and the store-operated Ca<sup>2+</sup> channel ORAI1 (Kar et al., 2014). The RII IS phosphorylation site  
497 is conserved throughout the animal kingdom, and co-anchoring of phosphatases alongside PKA is a feature  
498 of several AKAP complexes (Redden & Dodge-Kafka, 2011). Future investigations may therefore explore  
499 whether additional anchoring proteins are able to direct CN – or other cellular phosphatases – for direct  
500 suppression of PKA activity.

## 501 **Methods & Materials**

502

503 **Protein expression and purification.** Human PKA subunits were expressed and purified as described  
504 previously (Walker-Gray et al., 2017). GST-RII $\alpha$  and GST-RII $\beta$  were expressed in *Escherichia coli* BL21  
505 Tuner (DE3) pLysS, and GST-C $\beta$  in *E. coli* BL21 (DE3) grown in LB. In all cases, protein expression was  
506 induced by addition of 0.5 mM isopropyl  $\beta$ -D-1-thiogalactopyranoside (IPTG), and bacteria were harvested  
507 following overnight incubation at 20 °C. Cell pellets were thawed and sonicated in glutathione sepharose  
508 binding buffer (20 mM HEPES pH 7.5, 500 mM NaCl, 1 mM DTT, 0.5 mM EDTA, 1 mM benzamidine,  
509 10 % glycerol) supplemented with 0.1 mg/mL lysozyme, and 0.1 % Igepal CA-630 (RII subunit preps only).  
510 Clarified lysates were incubated with glutathione sepharose 4B, and PKA subunits were eluted by overnight  
511 cleavage with PreScission protease thus removing N-terminal GST affinity tags. Finally, each subunit was  
512 purified using a HiLoad 16/600 Superdex 200 column connected in series with a GSTrap to remove residual  
513 GST using gel filtration buffer (20 mM HEPES pH 7.5, 150 mM NaCl, 5 % glycerol). S98A and S98E  
514 point mutations were introduced into RII $\alpha$  subunits by site-directed mutagenesis (SDM) with primer pairs  
515 hS98A\_F & R, and hS98E\_F & R. RII $\alpha$  variants were expressed and purified in the same way as the WT  
516 sequences.

517 Full-length human AKAP79 was cloned into pET28 using primers Nde1\_AKAP79\_1 and  
518 AKAP79\_427\_EcoRI for expression of N-terminally 6His-tagged protein. AKAP79 was expressed in 4 L  
519 BL21 Star (DE3) cells by overnight incubation at 37 °C in auto-induction media (AIM). PBS-washed  
520 bacterial pellets were resuspended in Talon binding buffer (30 mM Tris pH 8.0, 500 mM NaCl, 10 mM  
521 imidazole, 1 mM benzamidine) supplemented with 0.1 mg/mL lysozyme and one Complete EDTA-free  
522 protease inhibitor tablet (Roche) per 100 mL. Lysates were sonicated, clarified by centrifugation, and  
523 incubated with Talon Superflow resin for 2 hours prior to 3 x 10 mL washing in Talon binding buffer, and  
524 eluted with 2 x 2.5 mL Talon elution buffer (30 mM Tris, pH 7.0, 500 mM NaCl, 300 mM imidazole, 1  
525 mM benzamidine). Eluted protein was exchanged into Q buffer A (20 mM Tris pH 8, 20 mM NaCl, 1 mM  
526 EDTA, 2 mM DTT) using a HiPrep 26/10 desalting column to enable purification using a 1 mL Resource  
527 Q column. Each variant was eluted using a NaCl/pH gradient with Q buffer A and a steadily increasing  
528 proportion of Q buffer B (20 mM Tris pH 7, 500 mM NaCl, 1 mM EDTA, 2mM DTT). In the final step,  
529 peak fractions were pooled and buffer exchanged into gel filtration buffer. Residues 331-427 of AKAP79  
530 were cloned into pET28 using primers Nde1\_AKAP79\_331 and AKAP79\_427\_EcoRI for expression of  
531 the fragment AKAP79<sub>331-427</sub> bearing an N-terminal His tag. This construct was transformed into BL21 (DE3)  
532 cells, which were grown overnight at 37 °C in AIM. Lysis and metal affinity steps were as for full-length  
533 AKAP79 with the exception that Ni-NTA agarose (Life Technologies) was used in place of Talon resin.  
534 Following elution from Ni-NTA resin, the protein was purified by size exclusion using a HiLoad

535 16/600Superdex 200 pre-equilibrated in gel filtration buffer. To assemble complexes of full-length RII  
536 subunits and AKAP79<sub>c97</sub>, mixtures of the purified proteins were incubated on ice in gel filtration buffer for  
537 1 h with the AKAP fragment in a 2:1 molar excess. The complex was then separated from excess  
538 AKAP79<sub>c97</sub> by Superdex 200 size exclusion. pET28-AKAP79<sub>c97</sub> ΔCN was generated by performing PCR  
539 with an earlier construct lacking residues 337-343 as the template (Gold et al., 2011), whereas the ΔPKA  
540 variant (lacking residues 391-400) was generated by SDM with primers ΔPKA\_F & \_R. The two  
541 AKAP79<sub>c97</sub> deletion mutants were expressed and purified in the same way as the WT protein.

542 Human CN was expressed from a bicistronic pGEX6P1 vector (Gold et al., 2011) in *E. coli* BL21  
543 Tuner (DE3) pLysS cells. Protein expression was induced by overnight incubation at 37 °C in 4L AIM. CN  
544 was purified following the same protocol as full-length PKA RII subunits, with the final size exclusion step  
545 performed using gel filtration buffer supplemented with 1 mM DTT. Human CaM was expressed and  
546 purified as described previously (Patel et al., 2017). Briefly, untagged CaM was expressed in *E. coli* BL21  
547 (DE3) cells incubated overnight at 37 °C in AIM. CaM was initially purified using phenyl sepharose resin,  
548 then by ion exchange with a HiTrap Q HP column. Finally, CaM was exchanged into water and lyophilized  
549 prior to storage at -80 °C. For AKAR4 purification, an 8His epitope tag was ligated into pcDNA3.1-  
550 AKAR4-NES vector (Depry et al., 2011) (Addgene cat no. 64727) at the C-terminus of the sensor  
551 immediately prior to the nuclear export site using primers EcoI\_8HisNLS\_XbaI and  
552 XbaI\_8HisNLS\_EcoRI. The vector was transfected into 20 x 10 cm dishes of HEK293T cells cultured in  
553 DMEM using lipofectamine-2000 (Thermo Fisher Scientific). Cells were collected after 3 days, washed in  
554 PBS, then lysed in Talon binding buffer supplemented with 0.5 % Igepal CA-630, and sonicated briefly.  
555 AKAR4 was purified by affinity to Ni-NTA agarose following the same procedure as for AKAP79, and  
556 eluted protein was exchanged into gel filtration buffer, and aliquoted before storage at -80 °C. All  
557 purification columns and resins were purchased from GE Healthcare. All protein samples were concentrated  
558 using Vivaspin centrifugal concentrators (Sartorius). Denaturing gel electrophoresis was performed using  
559 NuPAGE 4-12 % Bis-Tris gels (Thermo Fisher Scientific), and protein concentrations were determined  
560 using the bicinchoninic acid (BCA) assay.

561

562 **Phosphatase assays.** CN substrates were prepared by phosphorylating PKA RII subunits at the  
563 autoinhibitory site with PKA C subunit and ATP( $\gamma$ -<sup>32</sup>P). To radiolabel RII $\alpha$ , RII $\beta$ , or the purified complexes  
564 of each isoform with AKAP79<sub>c97</sub>, 50  $\mu$ g of the relevant sample was incubated in 100  $\mu$ L with  
565 phosphorylation buffer (20 mM HEPES pH 7.5, 150 mM NaCl, 100  $\mu$ M cAMP, 5 mM MgCl<sub>2</sub>, 0.03  $\mu$ g/ $\mu$ L  
566 C subunit) supplemented with 42 pmol [<sup>32</sup>P- $\gamma$ ]-ATP at 3000 Ci/mmol and 10  $\mu$ M cold ATP. After 15 min  
567 incubation at 30 °C, reactions were supplemented with 10  $\mu$ M additional cold ATP. Following 15 min  
568 further incubation, reactions were finally supplemented up to 1 mM cold ATP for 10 min further incubation.



569 <sup>32</sup>P-labelled protein was immediately separated from free <sup>32</sup>P using Sephadex G-25 Medium equilibrated in  
570 phospho-substrate storage buffer (20 mM HEPES pH 7.5, 150 mM NaCl, 10 % glycerol, 0.1 mM EDTA).  
571 Additional cold phospho-labelled substrates were prepared using scaled-up reactions with 1 mM cold ATP  
572 for 30 min at 30 °C.

573 Phosphatase assays (final volume 50 µL per assay) were prepared by first mixing appropriate  
574 dilutions of pRII substrates and CN on ice in dilution buffer (25 mM Na HEPES pH 7.5, 150 mM NaCl) to  
575 a final volume of 35 µL. 10 µL of reaction buffer (25 mM Na HEPES pH 7.5, 150 mM NaCl, 25 mM  
576 MgCl<sub>2</sub>, 5 mM DTT, 0.5 mg/mL BSA, 1 mM EDTA) was then added before initiation of CN activity by  
577 addition of 5 µL activator mix (25 mM Na HEPES pH 7.5, 150 mM NaCl, 10 mM CaCl<sub>2</sub>, 50 µM CaM).  
578 Assays was terminated after 30-60 s at 30 °C by addition of 350 µL 30 % trichloroacetic acid (TCA).  
579 Samples were then incubated on ice for 1 h, and protein was pelleted by centrifugation at 31,360 × g for 15  
580 min at 2 °C. The separated supernatant and pellet were analyzed using a Beckman LS 6000SC scintillation  
581 counter to determine the fraction of phosphate released from the pRII substrate. Reaction conditions were  
582 optimized so that less than 10 % pRII was dephosphorylated in each assay. Assays were generally  
583 performed with 10 nM CN and terminated after 30 s, with the exception of measurements for pRIIα and  
584 pRIIβ (black lines, **Figure 1E & F**) where 60 s reactions containing 100 nM CN were used.

585  
586 **Quantitative immunoblotting of CA1 neuropil extracts.** Hippocampal slices were prepared from 18-day  
587 old male Sprague-Dawley rats. Rats were euthanized by cervical dislocation and 350 µm-thick hippocampal  
588 slices were collected using a Leica VT1200S microtome in ice-cold sucrose-based saline (189 mM sucrose,  
589 10 mM glucose, 3 mM KCl, 5 mM MgSO<sub>4</sub>, 26 mM NaHCO<sub>3</sub>, 1.25 mM NaH<sub>2</sub>PO<sub>4</sub>, 0.1 mM CaCl<sub>2</sub>, pH 7.4)  
590 saturated with 95% O<sub>2</sub>/5% CO<sub>2</sub>. Slices were next transferred to a storage chamber filled with artificial  
591 cerebrospinal fluid (aCSF; 124 mM NaCl, 3 mM KCl, 24 mM NaHCO<sub>3</sub>, 1.25 mM NaH<sub>2</sub>PO<sub>4</sub>, 1 mM MgSO<sub>4</sub>,  
592 10 mM glucose, 2 mM CaCl<sub>2</sub>, pH 7.4) saturated with 95% O<sub>2</sub>/5% CO<sub>2</sub> first for one hour at ~ 31 °C and at  
593 room temperature thereafter. For micro-dissection, slices were transferred onto a pre-chilled Sylgard-coated  
594 90-mm petri dish atop a dry ice/ethanol bath. The CA1 neuropil layer was micro-dissected using an angled  
595 micro-knife (Cajigas et al., 2012) by first cutting along the borders of the stratum pyramidale/stratum  
596 radiatum and the stratum lacunosum moleculare/hippocampal fissure. Subsequent lateral cuts at the CA2-  
597 CA1 and subiculum-CA1 borders completed the rectangular micro-slices. Micro-dissected neuropil slices  
598 were immediately snap frozen in liquid nitrogen and stored at -80 °C. To extract protein, neuropil slices (~  
599 15 per animal) were first pulverized with a micro-pestle then resuspended in a final volume of 300 µL  
600 extraction buffer (50 mM Tris-HCl, 50 mM NaF, 10 mM EGTA, 10 mM EDTA, 0.08 mM sodium  
601 molybdate, 5 mM sodium pyrophosphate, 1 mM penylmethylsulfonyl fluoride, 0.5 % mM Igepal CA-630,  
602 0.25% mM sodium deoxycholate, 4 mM para-nitrophenylphosphate, cOmplete EDTA-free protease

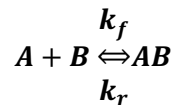
603 inhibitors and PhosStop phosphatase inhibitors (Roche) at 1 tablet each per 50 mL). The homogenate was  
604 sonicated briefly (30 s at 20 MHz) then clarified by centrifugation at 21,130 x g (15 min at 4 °C). Total  
605 protein concentration in each extract was determined by BCA assay. Quantitative immunoblotting was  
606 performed as described previously (Walker-Gray et al., 2017) using anti-PKA subunit primary antibodies  
607 purchased from BD Biosciences. HRP-conjugated secondary antibodies were detected with WesternBright  
608 ECL chemiluminescent HRP substrate using a ImageQuant imaging unit (GE Healthcare). Band intensities  
609 for reference protein standards and neuropil extracts were calculated in ImageJ. For each immunoblot, a  
610 reference curve was generated by fitting reference protein concentrations and band intensities to a Hill  
611 function (with typical  $R^2$  coefficients > 0.99) using iterative least squares refinement with the Levenberg-  
612 Marquardt algorithm in Origin (OriginLab). PKA subunit concentrations in neuropil extracts were  
613 determined by cross-referencing to reference curves derived from the same immunoblot.

614  
615 **AKAR4 measurements.** AKAR4 fluorescence measurements were performed using black-walled 96-well  
616 plates in a FLUOstar Omega microplate reader (BMG Labtech) equipped with a 430nm excitation filter,  
617 and 485nm/520nm emission filters. Each 50  $\mu$ L reaction contained 35  $\mu$ L proteins mixed in dilution buffer  
618 (20 mM HEPES pH 7.5 and 100 mM NaCl) including AKAR4 reporter (0.2  $\mu$ M final concentration in all  
619 cases) and 5  $\mu$ L of 10 x reaction buffer (20 mM Na HEPES pH 7.5, 100 mM NaCl, 10 mM DTT, 100 mM  
620 MgCl<sub>2</sub>, 10 mM CaCl<sub>2</sub>, 0.5 % Igepal CA-630). After three baseline measurements, PKA phosphorylation  
621 was initiated by addition of 10  $\mu$ L solution containing ATP and the desired concentration of cAMP using  
622 two injectors built into the plate reader. One injector was primed with ATP solution (20 mM Na HEPES  
623 pH 7.5, 100 mM NaCl, 25 mM ATP) and the other with ATP/cAMP solution (20 mM Na HEPES pH 7.5,  
624 100 mM NaCl, 25 mM ATP, 2.5 or 10  $\mu$ M cAMP) so that different proportions of the two injectors could  
625 be used to vary the final cAMP concentration. Measurements were collected at 5 second intervals for a  
626 minimum of 10 minutes at 22 °C following injection of ATP. For every run, one control well was included  
627 in which AKAR4 was omitted from the protein mixture to enable baseline subtraction. Run parameters  
628 were set using Reader Control Software for FLUOstar Omega, and measurements were analyzed using  
629 MARS Data Analysis Software (BMG Labtech). Aliquots of a single AKAR4 purification were used across  
630 all experiments.

631  
632 **Kinetic modeling.** The model scheme of PKA activation is an updated and extended version of the one  
633 published by Buxbaum and Dudai (Buxbaum & Dudai, 1989). The model was simulated in a single reaction  
634 compartment devoid of any geometry as a system of chemical reactions mimicking the experimental  
635 conditions listed above. The individual chemical reactions were modeled as ordinary differential equation  
636 (ODE) using the chemical mass-action equation, as:

637

638



639

640

$$-\frac{d[A]}{dt} = -\frac{d[B]}{dt} = \frac{d[AB]}{dt} = k_f(x) = k_f[A][B] = k_r[AB]$$

641

642 In total, there were 16 chemical species and 16 reactions included in the model, incorporating mostly bi-  
643 molecular reactions with forward and backward reaction rates. Enzymatic reactions were represented by  
644 the three elementary steps of binding, dissociation and catalysis. All model variants were built using the  
645 MATLAB Simbiology toolbox (MathWorks). All reactions, along with initial concentrations of all  
646 chemical species and kinetic rates, are listed in *Supplementary Table 1*.

647 PKA activation follows a sequential binding of four cAMP molecules to the PKA regulatory RII  
648 subunit holoenzyme followed by the release (or activation) of two active catalytic subunits (Taylor et al.,  
649 2019). However, the chosen modeling approach involved some simplifications: (1) The two RII subunits  
650 within the holoenzyme were assumed to behave independently – whereas in reality, some cooperativity is  
651 observed in PKA activation due to intra-dimeric contacts within the PKA holoenzymes (Taylor et al., 2012);  
652 (2) The two cAMP binding sites on the RII subunit were modelled as a single binding event such that  
653 binding of cAMP to RII/pRII is first order with respect to cAMP (Hao et al., 2019). This simplification was  
654 incorporated as our focus here was on understanding transitions between pRII and RII subunits and not the  
655 precise mechanism of cAMP activation; (3) The respective dephosphorylation parameters for both pRII and  
656 pRII bound to cAMP were assumed to be equal; (4) Rates of RII phosphorylation by bound C subunit were  
657 assumed to be equal irrespective of whether cAMP was bound to the regulatory subunit; (5) RII $\alpha$  and RII $\beta$   
658 were assumed to behave similarly since isoform-specific differences were not the focus here. These  
659 simplifications were used to reduce the number of model parameters.

660 Parameters corresponding to the reactions involving dephosphorylation by CN were modified to  
661 represent the situations ‘with’ and ‘without’ AKAP79 (*Supplementary Table 1*). In total twelve different  
662 experimental AKAR4 responses were used to estimate the model parameters. Six corresponded to data  
663 shown in *Figure 3C & E* collected with either 1 or 2  $\mu$ M cAMP activation: conditions with PKA (II) +  
664 CaM either alone, with CN, or with both CN and AKAP79. The other six correspond to the calibration  
665 curves of C subunit interaction with AKAR4 (*Figure 3-figure supplement 1A*), which were used to  
666 estimate AKAR4 parameters that were kept frozen when the other model parameters were estimated. All  
667 parameters were estimated using an approximate Bayesian computation (ABC) approach, which included  
668 copulas for merging of different experimental data sets (Eriksson et al., 2019). A Bayesian approach was

669 used over optimization for a single parameter set, to account for the uncertainty in parameter space, and  
670 that more than one set of parameters could fit the data. The result is thus described using distributions for  
671 possible parameter values, rather than single values. Initial prior knowledge about the possible parameter  
672 ranges using data from this study, and previously published work from other groups (Buxbaum & Dudai,  
673 1989; Isensee et al., 2018; Moore et al., 2003; Ogreid & Doskeland, 1981; Stemmer & Klee, 1994; Zhang  
674 et al., 2015; Zhang et al., 2012), was used to initiate the parameter fitting (details in *Supplementary Table*  
675 *I*). This was formalized as using a log uniform prior distribution for the ABC-method. Many of the  
676 parameters were set to have a 'prior' range which varied two orders of magnitude from a default parameter  
677 value (black bar in *Figure 5-figure supplement 1A*). For each parameter value, the default parameter value  
678 was retrieved from the literature or measurements performed in this study (*Supplementary Table 1*).  
679 Simulations were started with initial conditions mimicking the experimental settings, thus for the WT  
680 system the initial conditions were assumed to reflect that all RII were either free or bound to C with no  
681 phosphorylated species or interactions with cAMP. Simulations were then run for the same length as time  
682 as the experiments, assuming the cAMP was added at  $t=0$  and that autophosphorylation started at that time.

683 For predicting responses with mutant RII $\alpha$  subunits, the base model was extended by splitting the  
684 RII into two pools, namely RII $\alpha$  (85%) and RII $\beta$  (15%) but keeping the parameter distribution received  
685 from the parameter estimation when only one isoform of RII was accounted for. Experiments with WT RII  
686 subunits were successfully re-simulated with the extended model to validate the approach. As the mutations  
687 when simulating both S98A and S98E were in the RII $\alpha$  subtype (85%), the corresponding parameters  
688 depicting the mutation were only varied for this pool. Both the mutant forms, S98A and S98E, were tested  
689 as different model variants. To mimic the conditions of the S98A mutation in the model, the  
690 phosphorylation rates of RII $\alpha$  and RII $\alpha$  bound with cAMP were set to zero (i.e. for the RII $\alpha$  partition of  
691 the model, kinetics were restricted to the right-hand square sub-system shown in *Figure 4D*). Here the  
692 initial conditions were estimated in the same way as described above. To mimic the S98E mutation in the  
693 model, the turnover number for dephosphorylation of pRII $\alpha$  and pRII $\alpha$  with cAMP by CN were set to zero  
694 (i.e. for the RII $\alpha$  partition of the model, kinetics were restricted to the left-hand square in *Figure 4D*). Since  
695 S98E mimics a case where all the RII subunits are phosphorylated, in this case initial conditions were such  
696 that all RII $\alpha$  were distributed between pRII $\alpha$  and pRII $\alpha$ -C.

697 All model variants were built using the MATLAB Simbiology toolbox (MathWorks). Simulations  
698 of these reaction systems were performed using the ode15s solver. All simulations were run for 605 s and  
699 the AKAR4 phosphorylation was extracted as output to compare with the experimental findings. The model  
700 equations were also exported to the statistical programming language R (<https://www.r-project.org/>) for  
701 implementing the parameter estimation through the ABC-copula approach (Eriksson et al., 2019) and only  
702 accept parameter sets whose simulated phosphorylated AKAR4 curves reproduced the experimental

703 measurements. A slight modification to the distance measure  $\rho$  was, however, introduced to include  
704 timeseries data. The sampling was terminated when it had reached approximately 10,000 parameter samples  
705 (a subset of which are shown in *Figure 5-figure supplement 1A*) which all fitted the experimental data  
706 within a threshold set to  $\rho < 0.01$ . All parameter set samples, describing the uncertainty in the parameter  
707 estimates, were next projected onto the situations with mutant RII $\alpha$  subunits. The model immediately  
708 reproduced the experimental observations with RII $\alpha$  S98E subunits. Although the model correctly  
709 reproduced lower rates of AKAR4 that occur with RII $\alpha$  S98A subunits, and that suppression of PKA activity  
710 by AKAP79/CN is reduced in this case, there was a substantial spread in the simulated responses in this  
711 case. This indicated that WT data had not perfectly constrained the dynamics in the unphosphorylated RII  
712 sub-system (right-hand square, *Figure 4B*). Therefore, to better understand which parameter characteristics  
713 that were important to also account for the RII $\alpha$  S98A, the parameter sets were sub-classified based on how  
714 well they fit data collected with RII $\alpha$  S98A subunits and no CN (light red, *Figure 5C*) using a threshold of  
715 0.03. The parameter sets and its effect on different chemical species of the model were described by multi-  
716 trajectory, pairwise coordinate and boxplots, where the color schemes follow the classification described  
717 above. A code repository for this study may be accessed at  
718 <https://drive.google.com/drive/folders/1rNP7jDsLhWpCd8r7vt-eKUCf0eJSchT9>.

719

720 **Lentivirus construction.** Lentiviruses were generated by inserting RII $\alpha$ -IRES2-GFP expression cassettes  
721 into a pFUGW-H1 lentiviral vector (Addgene cat no. 25870) containing a shRNA sequence targeting for  
722 rat RII $\alpha$ . In the first step, coding sequence for rat PKA RII $\alpha$  was isolated from a cDNA library that we  
723 generated from total hippocampal RNA from a 7-day old male Sprague Dawley rat bred in the UCL colony.  
724 RNA was extracted using an RNeasy Mini Kit before the cDNA library was generated using the first-strand  
725 cDNA synthesis kit. Coding sequence for RII $\alpha$  was amplified from the library using primers Prkar2a\_F &  
726 Prkar2a\_R and inserted upstream of the IRES2 sequence in pIRES2-GFP (Clontech) using EcoRI and  
727 BamHI entry sites. Three pFUGW-H1-shRII $\alpha$  vectors were constructed to determine an optimal targeting  
728 sequence for knockdown of rat RII $\alpha$ . The targeting sequences (primer pairs shRII $\alpha$ \_F1/R1, shRII $\alpha$ \_F2/R2,  
729 and shRII $\alpha$ \_F3/R3) were inserted using the XbaI site of pFUGW-H1. The efficiency of each targeting  
730 sequence was determined by co-transfecting HEK293T cells with pIRES2-RII $\alpha$ -EGFP and each pFUGW-  
731 H1 vector, with the pFUGW vector in a 10-fold excess. Anti-RII $\alpha$  immunoblotting revealed that sequence  
732 shRII $\alpha$ -1, which targets bases 134-154 in the rat RII $\alpha$  coding sequence, was particularly effective at  
733 knocking down RII $\alpha$  protein levels (*Figure 6B*) so this variant served as the parent pFUGW-H1-shRII $\alpha$   
734 vector in the subsequent steps. The coding sequence for RII $\alpha$  in pIRES2-RII $\alpha$ -GFP was rendered shRNA-  
735 resistant ('RII $\alpha$ \*') by SDM with primers Prkar2a\_shRNA\_resist\_F & R. After introducing an NheI entry



736 site into pFUGW-H1-shRii $\alpha$  by SDM using primers FUGW\_NheI\_F & R, the dual expression cassette for  
737 Rii $\alpha$ -IRES2-GFP was transferred across into pFUGW-H1-shRii $\alpha$  downstream of the ubiquitin promoter  
738 using NheI and AgeI sites to create the complete lentiviral vector pFUGW-H1-shRii $\alpha$ -Rii $\alpha$ \*-IRES2-EGFP.

739 Vectors containing Rii $\alpha$  replacement sequences with mutations at S97 were obtained by SDM with  
740 primers pairs rS97A\_F & R and rS97E\_F & R. In addition, a control vector containing a scrambled shRNA  
741 sequence was constructed using primers shScram\_F & R. To produce lentivirus, pFUGW vectors were co-  
742 transfected with pCMVdR8.74 packaging vector (Addgene cat no. 12259) and pMD2.G envelope  
743 glycoprotein vector (Addgene cat no. 12259) into HEK293 cells using Lipofectamine 2000 and maintained  
744 in DMEM supplemented with 10% FBS. Cell culture media was collected at both 48 and 72 hours after  
745 transfection, subjected to 0.45  $\mu$ m filtering, and centrifuged at 48,384 x g for 4 hours at 4°C to concentrate  
746 viral particles. Pelleted virus was resuspended in sterile PBS and stored at - 80 °C. Lentiviruses were  
747 validated by transducing dissociated hippocampal cultures on DIV7. Neurons were collected on DIV14,  
748 and protein extracted using sonication (3 x 10 s at 20 MHz) in extraction buffer. The homogenate was  
749 clarified by centrifugation at 21,130 x g for 15 minutes before analysis of protein levels in the supernatant  
750 by immunoblotting using antibodies including anti-PKA pRii $\alpha$  (Abcam, RRID: AB\_779040), anti-GFP  
751 (Sigma Aldrich, RRID: AB\_2750576), and anti- $\beta$ -tubulin antibodies (Biolegend, RRID: AB\_2565030).

752

753 **Lentiviral infection and imaging of dissociated primary hippocampal neurons.** Primary hippocampal  
754 cultures were cultured from E18 Sprague-Dawley pups. Hippocampi were isolated and triturated with  
755 trypsin (0.025%) before plating on poly-L-lysine-coated coverslips or 6-well plates in DMEM containing  
756 10% heat-inactivated horse serum, and penicillin (40 U/mL)/streptomycin (40  $\mu$ g/mL). Neurons were  
757 cultured at 37°C in 95% air/5% CO<sub>2</sub>. Two hours after seeding, the plating media was replaced with  
758 Neurobasal-A supplemented with 1% B27, 0.5% (v/v) GlutaMAX, 20 mM glucose, and penicillin (100  
759 U/mL)/streptomycin (100  $\mu$ g/mL). Culture media and additives were purchased from Gibco with the  
760 exception of GlutaMAX (Thermo Fisher Scientific). Neurons were infected with lentivirus at DIV7 or DIV9  
761 for dendritic spine density and time-lapse experiments, respectively. Concentrated viral stocks were diluted  
762 in conditioned media and incubated with neurons for 18 hours before replacing with fresh pre-conditioned  
763 media. Live-cell confocal imaging of dendritic spines was performed using an upright Zeiss LSM 510  
764 confocal microscope equipped with an Achromplan 40x water differential interference contrast objective  
765 (numerical aperture 0.8). Transduced neurons were washed four times in HEPES-buffered Krebs solution  
766 (140 mM NaCl, 4.2 mM KCl, 1.2 mM MgCl<sub>2</sub>, 2.52 mM CaCl<sub>2</sub>, 5 mM Na HEPES, and 11 mM glucose,  
767 adjusted to pH 7.4 with NaOH) and placed into a chamber in this same solution at room temperature. For  
768 each dendritic segment, upper and lower bounds in the z-plane were initially determined using a rapid z-  
769 scan. A full image stack was then collected using a 488 nm Argon laser and a 505-530 nm band-pass



770 emission filter for imaging EGFP fluorescence using 512 x 512 frames with 3-line averaging, and optical  
771 slice spacing of 1.035  $\mu\text{m}$ . Time-lapse experiments were conducted to measure changes in spine density  
772 and spine-head size after the induction of chemical LTD. An optical slice spacing of 0.9  $\mu\text{m}$  was used  
773 during time-lapse experiments. Z-stacks were acquired every 5 min from 15 min before to 60 min after the  
774 induction of chemical LTD. Bath application of 20  $\mu\text{M}$  NMDA for 3 min was used to induce NMDAR-  
775 dependent LTD (Lee et al., 1998). Data was deconvolved using ImageJ (NIH) before automated dendrite  
776 identification and classification in NeuronStudio (Rodriguez et al., 2008). In time-lapse experiments,  
777 dendritic spine densities were normalized to the value at  $t=0$ .

778

779 **Statistical analysis.** All data are presented as means  $\pm$  SE. Kinetic rates were statistically compared using  
780 two-tailed unpaired Student *t*-tests. Spine imaging data was compared by ANOVA with Turkey post-hoc  
781 tests (**Figure 6D**) and Bonferroni's post-hoc test (**Figure 6G**). \* $p < 0.05$ ; \*\* $p < 0.01$ ; \*\*\* $p < 0.001$ .

782

783

## 784 **Author Contributions**

785 T.C. performed CA1 neuropil dissections, quantitative immunoblots, developed the lentiviral targeting  
786 vectors, and imaged structural plasticity in dendrites. P.T. J.A, O.E and J.H.K. built and simulated the  
787 AKAP79-PKA-CN signaling model. S.H. imaged and analyzed spine numbers in primary hippocampal  
788 neurons with support from T.G.S. M.G.G. conceived the study, purified proteins, and performed and  
789 analyzed phosphatase assays and AKAR4 recordings. M.G.G. and T.C. wrote the manuscript with input  
790 from all the authors.

791

## 792 **Acknowledgements**

793 We thank Denis Yuan for assistance with protein purification, and Alexandra Jauhiainen, Andrei Kramer  
794 and Federica Milinanni for help with the parameter estimation process. MGG is a Wellcome Trust and  
795 Royal Society Sir Henry Dale fellow (104194/Z/14/A), and is grateful for support from the BBSRC  
796 (BB/N015274/1). SH is a Rett Syndrome Fellow and also supported by a Wellcome Trust Collaborative  
797 award to TGS. The research was supported by the Swedish Research Council (VR-M-2017-02806), the  
798 Swedish e-Science Research Centre (SeRC), European Union/Horizon 2020 no. 945539 Human Brain  
799 Project SGA3, and an Erasmus Scholarship from Portugal. Optimizations and simulations were performed  
800 on resources provided by the Swedish National Infrastructure for Computing (SNIC) at Lunarc, Lund  
801 University.

802

## 803 References

804

805 Aye, T. T., Scholten, A., Taouatas, N., Varro, A., Van Veen, T. A., Vos, M. A., & Heck, A. J. (2010,  
806 Oct). Proteome-wide protein concentrations in the human heart. *Mol Biosyst*, 6(10), 1917-1927.  
807 <https://doi.org/10.1039/c004495d>  
808

809 Baillie, G. S., Tejada, G. S., & Kelly, M. P. (2019, Oct). Therapeutic targeting of 3',5'-cyclic nucleotide  
810 phosphodiesterases: inhibition and beyond. *Nat Rev Drug Discov*, 18(10), 770-796.  
811 <https://doi.org/10.1038/s41573-019-0033-4>  
812

813 Baldwin, T. A., & Dessauer, C. W. (2018, Jan 16). Function of Adenylyl Cyclase in Heart: the AKAP  
814 Connection. *J Cardiovasc Dev Dis*, 5(1). <https://doi.org/10.3390/jcdd5010002>  
815

816 Bear, M. F. (2003, Apr 29). Bidirectional synaptic plasticity: from theory to reality. *Philos Trans R Soc  
817 Lond B Biol Sci*, 358(1432), 649-655. <https://doi.org/10.1098/rstb.2002.1255>  
818

819 Bers, D. M., Xiang, Y. K., & Zaccolo, M. (2019, Jul 1). Whole-Cell cAMP and PKA Activity are  
820 Epiphenomena, Nanodomain Signaling Matters. *Physiology (Bethesda)*, 34(4), 240-249.  
821 <https://doi.org/10.1152/physiol.00002.2019>  
822

823 Bock, A., Annibale, P., Konrad, C., Hannawacker, A., Anton, S. E., Maiellaro, I., Zabel, U.,  
824 Sivaramakrishnan, S., Falcke, M., & Lohse, M. J. (2020, Sep 17). Optical Mapping of cAMP  
825 Signaling at the Nanometer Scale. *Cell*, 182(6), 1519-1530 e1517.  
826 <https://doi.org/10.1016/j.cell.2020.07.035>  
827

828 Buxbaum, J. D., & Dudai, Y. (1989, Jun 5). A quantitative model for the kinetics of cAMP-dependent  
829 protein kinase (type II) activity. Long-term activation of the kinase and its possible relevance to  
830 learning and memory. *J Biol Chem*, 264(16), 9344-9351.  
831 <https://www.ncbi.nlm.nih.gov/pubmed/2722837>  
832

833 Cajigas, I. J., Tushev, G., Will, T. J., tom Dieck, S., Fuerst, N., & Schuman, E. M. (2012, May 10). The  
834 local transcriptome in the synaptic neuropil revealed by deep sequencing and high-resolution  
835 imaging. *Neuron*, 74(3), 453-466. <https://doi.org/10.1016/j.neuron.2012.02.036>  
836

837 Clouet, D. H., & Gaitonde, M. K. (1956, Dec). The changes with age in the protein composition of the rat  
838 brain. *J Neurochem*, 1(2), 126-133. <https://doi.org/10.1111/j.1471-4159.1956.tb12063.x>  
839

840 Coghlan, V. M., Perrino, B. A., Howard, M., Langeberg, L. K., Hicks, J. B., Gallatin, W. M., & Scott, J.  
841 D. (1995, Jan 6). Association of protein kinase A and protein phosphatase 2B with a common  
842 anchoring protein. *Science*, 267(5194), 108-111.

- 843 [http://www.ncbi.nlm.nih.gov/entrez/query.fcgi?cmd=Retrieve&db=PubMed&dopt=Citation&list](http://www.ncbi.nlm.nih.gov/entrez/query.fcgi?cmd=Retrieve&db=PubMed&dopt=Citation&list_uids=7528941)  
844 [\\_uids=7528941](http://www.ncbi.nlm.nih.gov/entrez/query.fcgi?cmd=Retrieve&db=PubMed&dopt=Citation&list_uids=7528941)  
845
- 846 Dacher, M., Gouty, S., Dash, S., Cox, B. M., & Nugent, F. S. (2013, Feb 6). A-kinase anchoring protein-  
847 calcineurin signaling in long-term depression of GABAergic synapses. *J Neurosci*, 33(6), 2650-  
848 2660. <https://doi.org/10.1523/JNEUROSCI.2037-12.2013>  
849
- 850 Delint-Ramirez, I., Willoughby, D., Hammond, G. R., Ayling, L. J., & Cooper, D. M. (2011, Sep 23).  
851 Palmitoylation targets AKAP79 protein to lipid rafts and promotes its regulation of calcium-  
852 sensitive adenylyl cyclase type 8. *J Biol Chem*, 286(38), 32962-32975.  
853 <https://doi.org/10.1074/jbc.M111.243899>  
854
- 855 Dell'Acqua, M. L., Dodge, K. L., Tavalin, S. J., & Scott, J. D. (2002, Dec 13). Mapping the protein  
856 phosphatase-2B anchoring site on AKAP79. Binding and inhibition of phosphatase activity are  
857 mediated by residues 315-360. *J Biol Chem*, 277(50), 48796-48802.  
858 <https://doi.org/10.1074/jbc.M207833200>  
859
- 860 Dell'Acqua, M. L., Faux, M. C., Thorburn, J., Thorburn, A., & Scott, J. D. (1998, Apr 15). Membrane-  
861 targeting sequences on AKAP79 bind phosphatidylinositol-4, 5-bisphosphate. *Embo J*, 17(8),  
862 2246-2260.  
863 [http://www.ncbi.nlm.nih.gov/entrez/query.fcgi?cmd=Retrieve&db=PubMed&dopt=Citation&list](http://www.ncbi.nlm.nih.gov/entrez/query.fcgi?cmd=Retrieve&db=PubMed&dopt=Citation&list_uids=9545238)  
864 [\\_uids=9545238](http://www.ncbi.nlm.nih.gov/entrez/query.fcgi?cmd=Retrieve&db=PubMed&dopt=Citation&list_uids=9545238)  
865
- 866 Depry, C., Allen, M. D., & Zhang, J. (2011, Jan). Visualization of PKA activity in plasma membrane  
867 microdomains [Research Support, N.I.H., Extramural]. *Mol Biosyst*, 7(1), 52-58.  
868 <https://doi.org/10.1039/c0mb00079e>  
869
- 870 Dittmer, P. J., Dell'Acqua, M. L., & Sather, W. A. (2014, Jun 12). Ca<sup>2+</sup>/calcineurin-dependent  
871 inactivation of neuronal L-type Ca<sup>2+</sup> channels requires priming by AKAP-anchored protein  
872 kinase A. *Cell Rep*, 7(5), 1410-1416. <https://doi.org/10.1016/j.celrep.2014.04.039>  
873
- 874 Eriksson, O., Jauhiainen, A., Maad Sasane, S., Kramer, A., Nair, A. G., Sartorius, C., & Hellgren  
875 Kotaleski, J. (2019, Jan 15). Uncertainty quantification, propagation and characterization by  
876 Bayesian analysis combined with global sensitivity analysis applied to dynamical intracellular  
877 pathway models. *Bioinformatics*, 35(2), 284-292. <https://doi.org/10.1093/bioinformatics/bty607>  
878
- 879 Gold, M. G. (2019, Oct 31). Swimming regulations for protein kinase A catalytic subunit. *Biochem Soc*  
880 *Trans*, 47(5), 1355-1366. <https://doi.org/10.1042/BST20190230>  
881
- 882 Gold, M. G., Lygren, B., Dokurno, P., Hoshi, N., McConnachie, G., Tasken, K., Carlson, C. R., Scott, J.  
883 D., & Barford, D. (2006). Molecular basis of AKAP specificity for PKA regulatory subunits.  
884 *Molecular cell*, 24(3), 383-395. <Go to ISI>://MEDLINE:17081989

885

886 Gold, M. G., Stengel, F., Nygren, P. J., Weisbrod, C. R., Bruce, J. E., Robinson, C. V., Barford, D., &  
887 Scott, J. D. (2011, Apr 19). Architecture and dynamics of an A-kinase anchoring protein 79  
888 (AKAP79) signaling complex. *Proc Natl Acad Sci U S A*, 108(16), 6426-6431.

889 <https://doi.org/10.1073/pnas.1014400108> [pii]

890 10.1073/pnas.1014400108

891

892 Hinke, S. A., Navedo, M. F., Ulman, A., Whiting, J. L., Nygren, P. J., Tian, G., Jimenez-Caliani, A. J.,  
893 Langeberg, L. K., Cirulli, V., Tengholm, A., Dell'Acqua, M. L., Santana, L. F., & Scott, J. D.  
894 (2012, Oct 17). Anchored phosphatases modulate glucose homeostasis. *Embo J*, 31(20), 3991-

895 4004. <https://doi.org/10.1038/emboj.2012.244>

896

897 Hogan, P. G. (2017, May). Calcium-NFAT transcriptional signalling in T cell activation and T cell  
898 exhaustion. *Cell Calcium*, 63, 66-69. <https://doi.org/10.1016/j.ceca.2017.01.014>

899

900 Hoshi, N., Langeberg, L. K., Gould, C. M., Newton, A. C., & Scott, J. D. (2010, Feb 26). Interaction with  
901 AKAP79 modifies the cellular pharmacology of PKC. *Molecular cell*, 37(4), 541-550.

902 <https://doi.org/10.1016/j.molcel.2010.01.014>

903

904 Houslay, M. D., & Baillie, G. S. (2005, Dec). Beta-arrestin-recruited phosphodiesterase-4 desensitizes the  
905 AKAP79/PKA-mediated switching of beta2-adrenoceptor signalling to activation of ERK.

906 *Biochem Soc Trans*, 33(Pt 6), 1333-1336. <https://doi.org/10.1042/BST20051333>

907

908 Huang, Y. Y., Li, X. C., & Kandel, E. R. (1994, Oct 7). cAMP contributes to mossy fiber LTP by  
909 initiating both a covalently mediated early phase and macromolecular synthesis-dependent late

910 phase. *Cell*, 79(1), 69-79. [https://doi.org/10.1016/0092-8674\(94\)90401-4](https://doi.org/10.1016/0092-8674(94)90401-4)

911

912 Ilouz, R., Lev-Ram, V., Bushong, E. A., Stiles, T. L., Friedmann-Morvinski, D., Douglas, C., Goldberg,  
913 G., Ellisman, M. H., & Taylor, S. S. (2017, Jan 12). Isoform-specific subcellular localization and  
914 function of protein kinase A identified by mosaic imaging of mouse brain. *Elife*, 6.

915 <https://doi.org/10.7554/eLife.17681>

916

917 Isensee, J., Kaufholz, M., Knape, M. J., Hasenauer, J., Hammerich, H., Gonczarowska-Jorge, H., Zahedi,  
918 R. P., Schwede, F., Herberg, F. W., & Hucho, T. (2018, Jun 4). PKA-RII subunit phosphorylation  
919 precedes activation by cAMP and regulates activity termination. *J Cell Biol*, 217(6), 2167-2184.

920 <https://doi.org/10.1083/jcb.201708053>

921

922 Jurado, S., Biou, V., & Malenka, R. C. (2010, Sep). A calcineurin/AKAP complex is required for NMDA  
923 receptor-dependent long-term depression. *Nat Neurosci*, 13(9), 1053-1055.

924 <https://doi.org/nm.2613> [pii]

925 10.1038/nm.2613

926

- 927 Kar, P., Samanta, K., Kramer, H., Morris, O., Bakowski, D., & Parekh, A. B. (2014, Jun 16). Dynamic  
928 assembly of a membrane signaling complex enables selective activation of NFAT by Orai1. *Curr*  
929 *Biol*, 24(12), 1361-1368. <https://doi.org/10.1016/j.cub.2014.04.046>  
930
- 931 Kashishian, A., Howard, M., Loh, C., Gallatin, W. M., Hoekstra, M. F., & Lai, Y. (1998, Oct 16).  
932 AKAP79 inhibits calcineurin through a site distinct from the immunophilin-binding region. *J Biol*  
933 *Chem*, 273(42), 27412-27419. <https://doi.org/10.1074/jbc.273.42.27412>  
934
- 935 Keith, D. J., Sanderson, J. L., Gibson, E. S., Woolfrey, K. M., Robertson, H. R., Olszewski, K., Kang, R.,  
936 El-Husseini, A., & Dell'acqua, M. L. (2012, May 23). Palmitoylation of A-kinase anchoring  
937 protein 79/150 regulates dendritic endosomal targeting and synaptic plasticity mechanisms. *J*  
938 *Neurosci*, 32(21), 7119-7136. <https://doi.org/10.1523/JNEUROSCI.0784-12.2012>  
939
- 940 Kinderman, F. S., Kim, C., von Daake, S., Ma, Y., Pham, B. Q., Spraggon, G., Xuong, N.-H., Jennings, P.  
941 A., & Taylor, S. S. (2006). A dynamic mechanism for AKAP binding to RII isoforms of cAMP-  
942 dependent protein kinase. *Molecular cell*, 24(3), 397-408. <Go to ISI>://MEDLINE:17081990  
943
- 944 Kwon, H. B., & Sabatini, B. L. (2011, Jun 2). Glutamate induces de novo growth of functional spines in  
945 developing cortex. *Nature*, 474(7349), 100-104. <https://doi.org/10.1038/nature09986>  
946
- 947 Lee, H. K., Kameyama, K., Huganir, R. L., & Bear, M. F. (1998, Nov). NMDA induces long-term  
948 synaptic depression and dephosphorylation of the GluR1 subunit of AMPA receptors in  
949 hippocampus. *Neuron*, 21(5), 1151-1162. [https://doi.org/10.1016/s0896-6273\(00\)80632-7](https://doi.org/10.1016/s0896-6273(00)80632-7)  
950
- 951 Li, H., Pink, M. D., Murphy, J. G., Stein, A., Dell'Acqua, M. L., & Hogan, P. G. (2012, Feb 19). Balanced  
952 interactions of calcineurin with AKAP79 regulate Ca<sup>2+</sup>-calcineurin-NFAT signaling. *Nat Struct*  
953 *Mol Biol*, 19(3), 337-345. <https://doi.org/10.1038/nsmb.2238>  
954
- 955 Lu, Y., Zha, X. M., Kim, E. Y., Schachtele, S., Dailey, M. E., Hall, D. D., Strack, S., Green, S. H.,  
956 Hoffman, D. A., & Hell, J. W. (2011, Jul 29). A kinase anchor protein 150 (AKAP150)-  
957 associated protein kinase A limits dendritic spine density. *J Biol Chem*, 286(30), 26496-26506.  
958 <https://doi.org/10.1074/jbc.M111.254912>  
959
- 960 Lu, Y., Zhang, M., Lim, I. A., Hall, D. D., Allen, M., Medvedeva, Y., McKnight, G. S., Usachev, Y. M.,  
961 & Hell, J. W. (2008, Sep 1). AKAP150-anchored PKA activity is important for LTD during its  
962 induction phase. *J Physiol*, 586(17), 4155-4164. <https://doi.org/10.1113/jphysiol.2008.151662>  
963
- 964 Moore, M. J., Adams, J. A., & Taylor, S. S. (2003, Mar 21). Structural basis for peptide binding in protein  
965 kinase A. Role of glutamic acid 203 and tyrosine 204 in the peptide-positioning loop. *J Biol*  
966 *Chem*, 278(12), 10613-10618. <https://doi.org/10.1074/jbc.M210807200>  
967

- 968 Mulkey, R. M., Endo, S., Shenolikar, S., & Malenka, R. C. (1994, Jun 9). Involvement of a  
969 calcineurin/inhibitor-1 phosphatase cascade in hippocampal long-term depression. *Nature*,  
970 369(6480), 486-488. <https://doi.org/10.1038/369486a0>  
971
- 972 Murphy, J. G., Sanderson, J. L., Gorski, J. A., Scott, J. D., Catterall, W. A., Sather, W. A., & Dell'Acqua,  
973 M. L. (2014, Jun 12). AKAP-anchored PKA maintains neuronal L-type calcium channel activity  
974 and NFAT transcriptional signaling. *Cell Rep*, 7(5), 1577-1588.  
975 <https://doi.org/10.1016/j.celrep.2014.04.027>  
976
- 977 Ni, Q., Ganesan, A., Aye-Han, N. N., Gao, X., Allen, M. D., Levchenko, A., & Zhang, J. (2011, Jan).  
978 Signaling diversity of PKA achieved via a Ca<sup>2+</sup>-cAMP-PKA oscillatory circuit. *Nat Chem Biol*,  
979 7(1), 34-40. <https://doi.org/10.1038/nchembio.478>  
980
- 981 Nygren, P. J., Mehta, S., Schweppe, D. K., Langeberg, L. K., Whiting, J. L., Weisbrod, C. R., Bruce, J.  
982 E., Zhang, J., Veessler, D., & Scott, J. D. (2017, Oct 2). Intrinsic disorder within AKAP79 fine-  
983 tunes anchored phosphatase activity toward substrates and drug sensitivity. *Elife*, 6.  
984 <https://doi.org/10.7554/eLife.30872>  
985
- 986 Ogreid, D., & Doskeland, S. O. (1981, Jul 6). The kinetics of the interaction between cyclic AMP and the  
987 regulatory moiety of protein kinase II. Evidence for interaction between the binding sites for  
988 cyclic AMP. *FEBS Lett*, 129(2), 282-286. <https://www.ncbi.nlm.nih.gov/pubmed/6269881>  
989
- 990 Patel, N., Stengel, F., Aebersold, R., & Gold, M. G. (2017, Nov 22). Molecular basis of AKAP79  
991 regulation by calmodulin. *Nat Commun*, 8(1), 1681. <https://doi.org/10.1038/s41467-017-01715-w>  
992
- 993 Perrino, B. A., Fong, Y. L., Brickey, D. A., Saitoh, Y., Ushio, Y., Fukunaga, K., Miyamoto, E., &  
994 Soderling, T. R. (1992, Aug 5). Characterization of the phosphatase activity of a baculovirus-  
995 expressed calcineurin A isoform. *J Biol Chem*, 267(22), 15965-15969.  
996 <https://www.ncbi.nlm.nih.gov/pubmed/1322410>  
997
- 998 Qi, C., Sorrentino, S., Medalia, O., & Korkhov, V. M. (2019, Apr 26). The structure of a membrane  
999 adenylyl cyclase bound to an activated stimulatory G protein. *Science*, 364(6438), 389-394.  
1000 <https://doi.org/10.1126/science.aav0778>  
1001
- 1002 Qian, H., Patriarchi, T., Price, J. L., Matt, L., Lee, B., Nieves-Cintrón, M., Buonarati, O. R., Chowdhury,  
1003 D., Nanou, E., Nystoriak, M. A., Catterall, W. A., Poomvanicha, M., Hofmann, F., Navedo, M.  
1004 F., & Hell, J. W. (2017, Jan 24). Phosphorylation of Ser1928 mediates the enhanced activity of  
1005 the L-type Ca<sup>2+</sup> channel Cav1.2 by the beta2-adrenergic receptor in neurons. *Sci Signal*, 10(463).  
1006 <https://doi.org/10.1126/scisignal.aaf9659>  
1007
- 1008 Rangel-Aldao, R., & Rosen, O. M. (1976, Jun 10). Dissociation and reassociation of the phosphorylated  
1009 and nonphosphorylated forms of adenosine 3':5' -monophosphate-dependent protein kinase from



- 1010 bovine cardiac muscle. *J Biol Chem*, 251(11), 3375-3380.  
1011 <https://www.ncbi.nlm.nih.gov/pubmed/179996>  
1012
- 1013 Redden, J. M., & Dodge-Kafka, K. L. (2011, Oct). AKAP phosphatase complexes in the heart. *J*  
1014 *Cardiovasc Pharmacol*, 58(4), 354-362. <https://doi.org/10.1097/FJC.0b013e31821e5649>  
1015
- 1016 Roach, P. J., Depaoli-Roach, A. A., Hurley, T. D., & Tagliabracci, V. S. (2012, Feb 1). Glycogen and its  
1017 metabolism: some new developments and old themes. *Biochem J*, 441(3), 763-787.  
1018 <https://doi.org/10.1042/BJ20111416>  
1019
- 1020 Rodriguez, A., Ehlenberger, D. B., Dickstein, D. L., Hof, P. R., & Wearne, S. L. (2008, Apr 23).  
1021 Automated three-dimensional detection and shape classification of dendritic spines from  
1022 fluorescence microscopy images. *PLoS One*, 3(4), e1997.  
1023 <https://doi.org/10.1371/journal.pone.0001997>  
1024
- 1025 Roy, J., & Cyert, M. S. (2009, Dec 8). Cracking the phosphatase code: docking interactions determine  
1026 substrate specificity. *Sci Signal*, 2(100), re9. <https://doi.org/10.1126/scisignal.2100re9>  
1027
- 1028 Sanderson, J. L., Gorski, J. A., & Dell'Acqua, M. L. (2016, Mar 2). NMDA Receptor-Dependent LTD  
1029 Requires Transient Synaptic Incorporation of Ca<sup>2+</sup>(+)-Permeable AMPARs Mediated by  
1030 AKAP150-Anchored PKA and Calcineurin. *Neuron*, 89(5), 1000-1015.  
1031 <https://doi.org/10.1016/j.neuron.2016.01.043>  
1032
- 1033 Sanderson, J. L., Gorski, J. A., Gibson, E. S., Lam, P., Freund, R. K., Chick, W. S., & Dell'Acqua, M. L.  
1034 (2012, Oct 24). AKAP150-anchored calcineurin regulates synaptic plasticity by limiting synaptic  
1035 incorporation of Ca<sup>2+</sup>-permeable AMPA receptors. *J Neurosci*, 32(43), 15036-15052.  
1036 <https://doi.org/10.1523/JNEUROSCI.3326-12.2012>  
1037
- 1038 Schmitt, J. P., Kamisago, M., Asahi, M., Li, G. H., Ahmad, F., Mende, U., Kranias, E. G., MacLennan, D.  
1039 H., Seidman, J. G., & Seidman, C. E. (2003, Feb 28). Dilated cardiomyopathy and heart failure  
1040 caused by a mutation in phospholamban. *Science*, 299(5611), 1410-1413.  
1041 <https://doi.org/10.1126/science.1081578>  
1042
- 1043 Stemmer, P. M., & Klee, C. B. (1994, Jun 7). Dual calcium ion regulation of calcineurin by calmodulin  
1044 and calcineurin B. *Biochemistry*, 33(22), 6859-6866. <https://doi.org/10.1021/bi00188a015>  
1045
- 1046 Taylor, S. S., Meharena, H. S., & Kornev, A. P. (2019, Jun). Evolution of a dynamic molecular switch.  
1047 *IUBMB Life*, 71(6), 672-684. <https://doi.org/10.1002/iub.2059>  
1048

- 1049 Tunquist, B. J., Hoshi, N., Guire, E. S., Zhang, F., Mullendorff, K., Langeberg, L. K., Raber, J., & Scott,  
1050 J. D. (2008, Aug 26). Loss of AKAP150 perturbs distinct neuronal processes in mice. *Proc Natl*  
1051 *Acad Sci U S A*, 105(34), 12557-12562. <https://doi.org/0805922105> [pii]  
1052 10.1073/pnas.0805922105  
1053
- 1054 Walker-Gray, R., Stengel, F., & Gold, M. G. (2017, Sep 26). Mechanisms for restraining cAMP-  
1055 dependent protein kinase revealed by subunit quantitation and cross-linking approaches. *Proc*  
1056 *Natl Acad Sci U S A*, 114(39), 10414-10419. <https://doi.org/10.1073/pnas.1701782114>  
1057
- 1058 Weisenhaus, M., Allen, M. L., Yang, L., Lu, Y., Nichols, C. B., Su, T., Hell, J. W., & McKnight, G. S.  
1059 (2010, Apr 23). Mutations in AKAP5 disrupt dendritic signaling complexes and lead to  
1060 electrophysiological and behavioral phenotypes in mice. *PLoS One*, 5(4), e10325.  
1061 <https://doi.org/10.1371/journal.pone.0010325>  
1062
- 1063 Wild, A. R., Sinnen, B. L., Dittmer, P. J., Kennedy, M. J., Sather, W. A., & Dell'Acqua, M. L. (2019, Mar  
1064 26). Synapse-to-Nucleus Communication through NFAT Is Mediated by L-type Ca(2+) Channel  
1065 Ca(2+) Spike Propagation to the Soma. *Cell Rep*, 26(13), 3537-3550 e3534.  
1066 <https://doi.org/10.1016/j.celrep.2019.03.005>  
1067
- 1068 Woolfrey, K. M., O'Leary, H., Goodell, D. J., Robertson, H. R., Horne, E. A., Coultrap, S. J., Dell'Acqua,  
1069 M. L., & Bayer, K. U. (2018, Feb 2). CaMKII regulates the depalmitoylation and synaptic  
1070 removal of the scaffold protein AKAP79/150 to mediate structural long-term depression. *J Biol*  
1071 *Chem*, 293(5), 1551-1567. <https://doi.org/10.1074/jbc.M117.813808>  
1072
- 1073 Zhang, J., & Shapiro, M. S. (2012, Dec 20). Activity-dependent transcriptional regulation of M-Type  
1074 (Kv7) K(+) channels by AKAP79/150-mediated NFAT actions. *Neuron*, 76(6), 1133-1146.  
1075 <https://doi.org/10.1016/j.neuron.2012.10.019>  
1076
- 1077 Zhang, J., & Shapiro, M. S. (2016, Jan 1). Mechanisms and dynamics of AKAP79/150-orchestrated  
1078 multi-protein signalling complexes in brain and peripheral nerve. *J Physiol*, 594(1), 31-37.  
1079 <https://doi.org/10.1113/jphysiol.2014.287698>  
1080
- 1081 Zhang, J. Z., Lu, T. W., Stolerman, L. M., Tenner, B., Yang, J. R., Zhang, J. F., Falcke, M., Rangamani,  
1082 P., Taylor, S. S., Mehta, S., & Zhang, J. (2020, Sep 17). Phase Separation of a PKA Regulatory  
1083 Subunit Controls cAMP Compartmentation and Oncogenic Signaling. *Cell*, 182(6), 1531-1544  
1084 e1515. <https://doi.org/10.1016/j.cell.2020.07.043>  
1085
- 1086 Zhang, P., Knape, M. J., Ahuja, L. G., Keshwani, M. M., King, C. C., Sastri, M., Herberg, F. W., &  
1087 Taylor, S. S. (2015). Single Turnover Autophosphorylation Cycle of the PKA RIIbeta  
1088 Holoenzyme. *PLoS biology*, 13(7), e1002192. <Go to ISI>://MEDLINE:26158466  
1089

- 1090 Zhang, P., Smith-Nguyen, E. V., Keshwani, M. M., Deal, M. S., Kornev, A. P., & Taylor, S. S. (2012,  
1091 Feb 10). Structure and allostery of the PKA RIIbeta tetrameric holoenzyme. *Science*, 335(6069),  
1092 712-716. <https://doi.org/10.1126/science.1213979>  
1093
- 1094 Zhang, X., Li, L., & McNaughton, P. A. (2008, Aug 14). Proinflammatory mediators modulate the heat-  
1095 activated ion channel TRPV1 via the scaffolding protein AKAP79/150. *Neuron*, 59(3), 450-461.  
1096 <https://doi.org/10.1016/j.neuron.2008.05.015>  
1097
- 1098 Zhang, X., Pathak, T., Yoast, R., Emrich, S., Xin, P., Nwokonko, R. M., Johnson, M., Wu, S., Delierneux,  
1099 C., Gueguinou, M., Hempel, N., Putney, J. W., Jr., Gill, D. L., & Trebak, M. (2019, Apr 29). A  
1100 calcium/cAMP signaling loop at the ORAI1 mouth drives channel inactivation to shape NFAT  
1101 induction. *Nat Commun*, 10(1), 1971. <https://doi.org/10.1038/s41467-019-09593-0>  
1102
- 1103 Zhou, Q., Homma, K. J., & Poo, M. M. (2004, Dec 2). Shrinkage of dendritic spines associated with long-  
1104 term depression of hippocampal synapses. *Neuron*, 44(5), 749-757.  
1105 <https://doi.org/10.1016/j.neuron.2004.11.011>  
1106
- 1107
- 1108

1109 **Supplementary Information**

1110

1111 **Figure 1-figure supplement 1.** Purified proteins.

1112

1113 **Figure 1-figure supplement 2.** pRII phosphorylation by CN at supra-physiological concentrations

1114

1115 **Figure 2-figure supplement 1.** Reference curves for quantitation of PKA subunits in CA1 neuropil

1116

1117 **Figure 3-figure supplement 1.** AKAR4 reference measurements with PKA catalytic subunit

1118

1119 **Figure 4-figure supplement 1.** Simulations of kinetic scheme species changes in concentration over time

1120

1121 **Figure 5-figure supplement 1.** Space of parameters used in model fitting

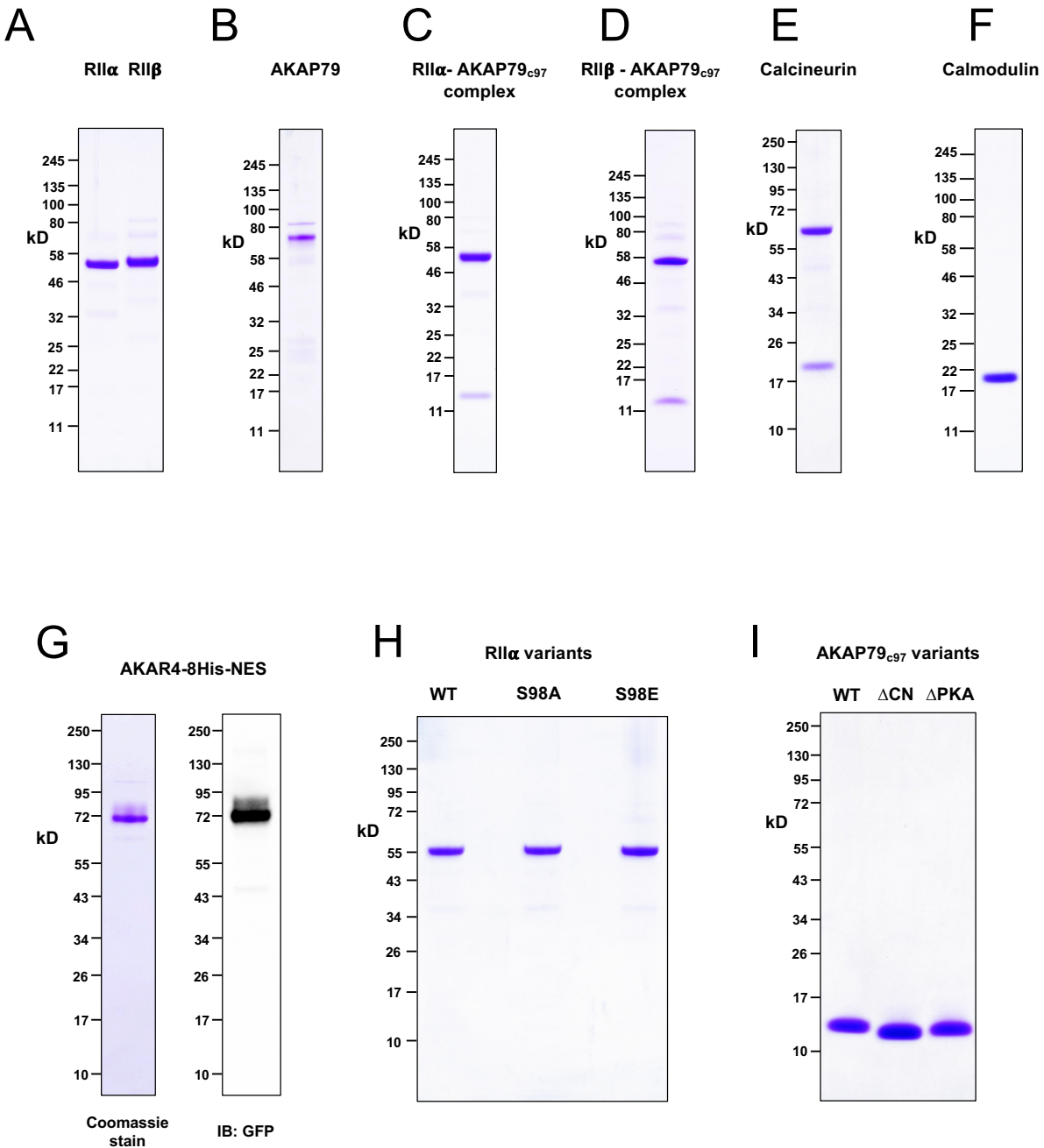
1122

1123 **Supplementary Table 1.** Kinetic modeling parameters

1124

1125 **Supplementary Table 2.** Oligonucleotide primer sequences

1126



1127

1128

1129

1130

1131

1132

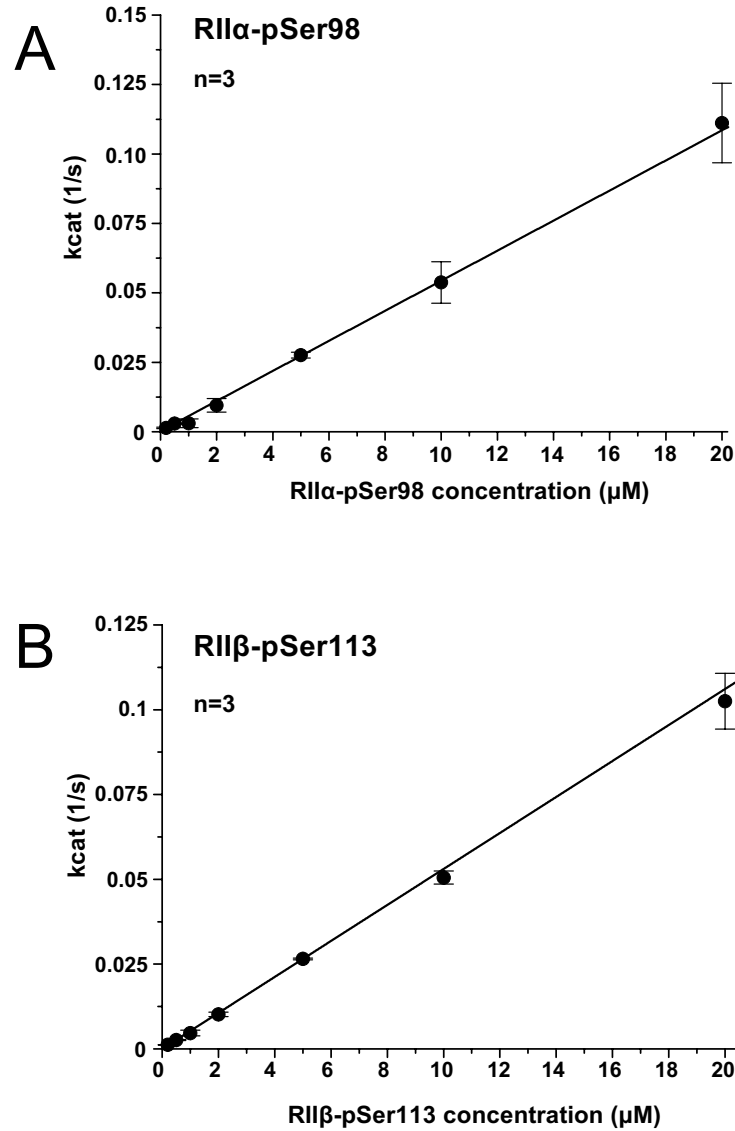
1133

1134

1135

**Figure 1-figure supplement 1. Purified proteins.** Images showing the purity of purified proteins applied in this study are shown following SDS-PAGE with 4–12% Bis-Tris NuPAGE gels. **(A)** Full-length WT PKA RII $\alpha$  and RII $\beta$  subunits. **(B)** Full-length AKAP79. **(C)** The complex of RII $\alpha$  and AKAP79<sub>c97</sub>. **(D)** The complex of RII $\beta$  and AKAP79<sub>c97</sub>. **(E)** The CN heterodimer. **(F)** CaM. **(G)** AKAR4 – the left-hand image shows Coomassie staining whereas the right-hand image shows anti-GFP immunoblotting of an equivalent lane after transfer to nitrocellulose. **(H)** Variants of RII $\alpha$  (WT, S98A, S98E) applied in AKAR4 assays. **(I)** Variants of AKAP79<sub>c97</sub> (WT,  $\Delta$ CN,  $\Delta$ PKA) applied in AKAR4 assays. All images were scanned following Coomassie staining unless otherwise stated.

1136



1137

1138

1139

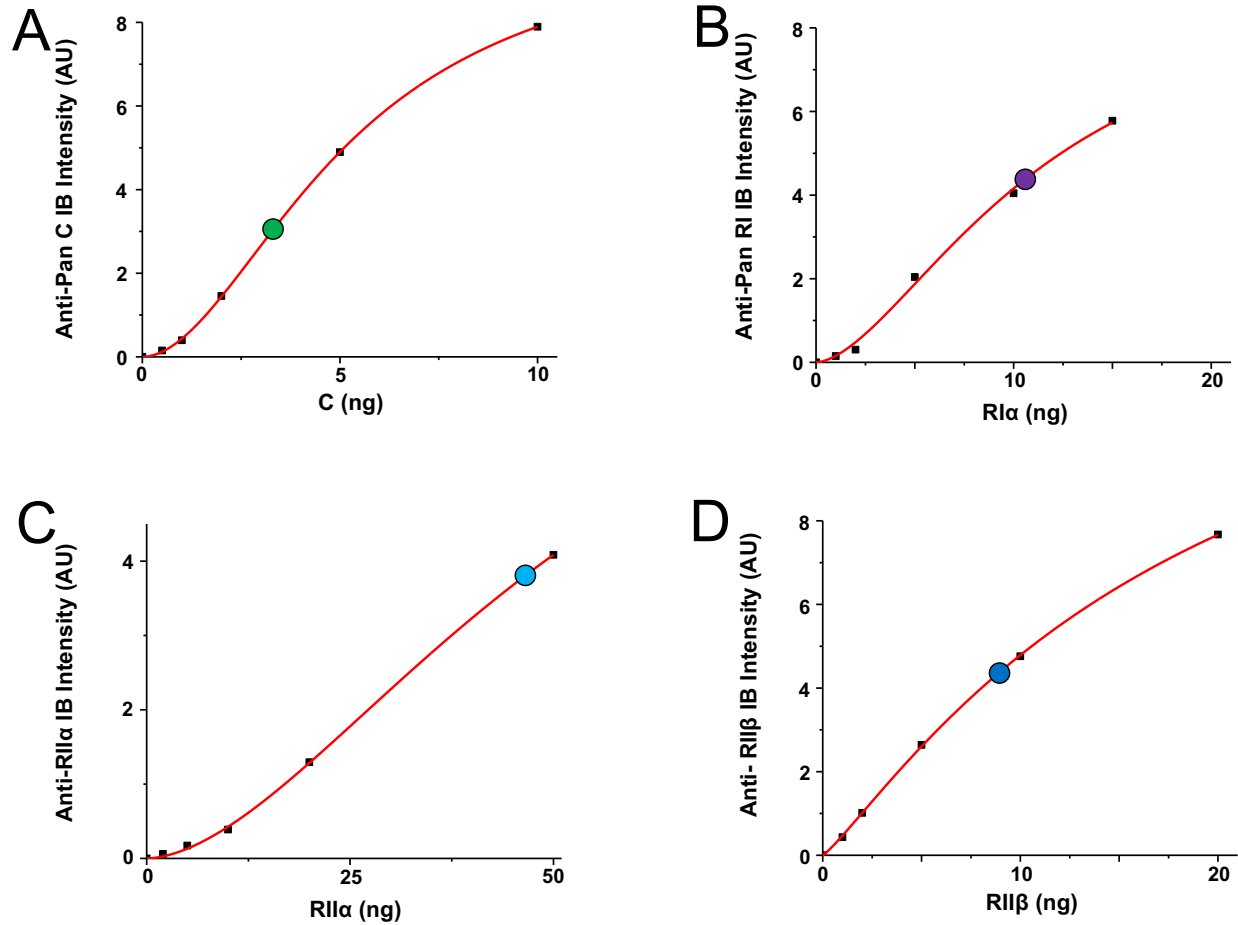
1140

1141

1142

**Figure 1-figure supplement 2. pRII phosphorylation by CN at supra-physiological concentrations.** The relationship between CN activity towards pRII and pRII concentration in the absence of AKAP79 is linear for both pRII $\alpha$  (**A**) and pRII $\beta$  (**B**) up to at least 20  $\mu$ M pRII.





1143

1144

1145

1146 **Figure 2-figure supplement 1. Reference curves for quantitation of PKA subunits in CA1 neuropil.** The

1147 four panels show reference curves (red lines) that relate immunoblot band intensity to ng of PKA subunit per

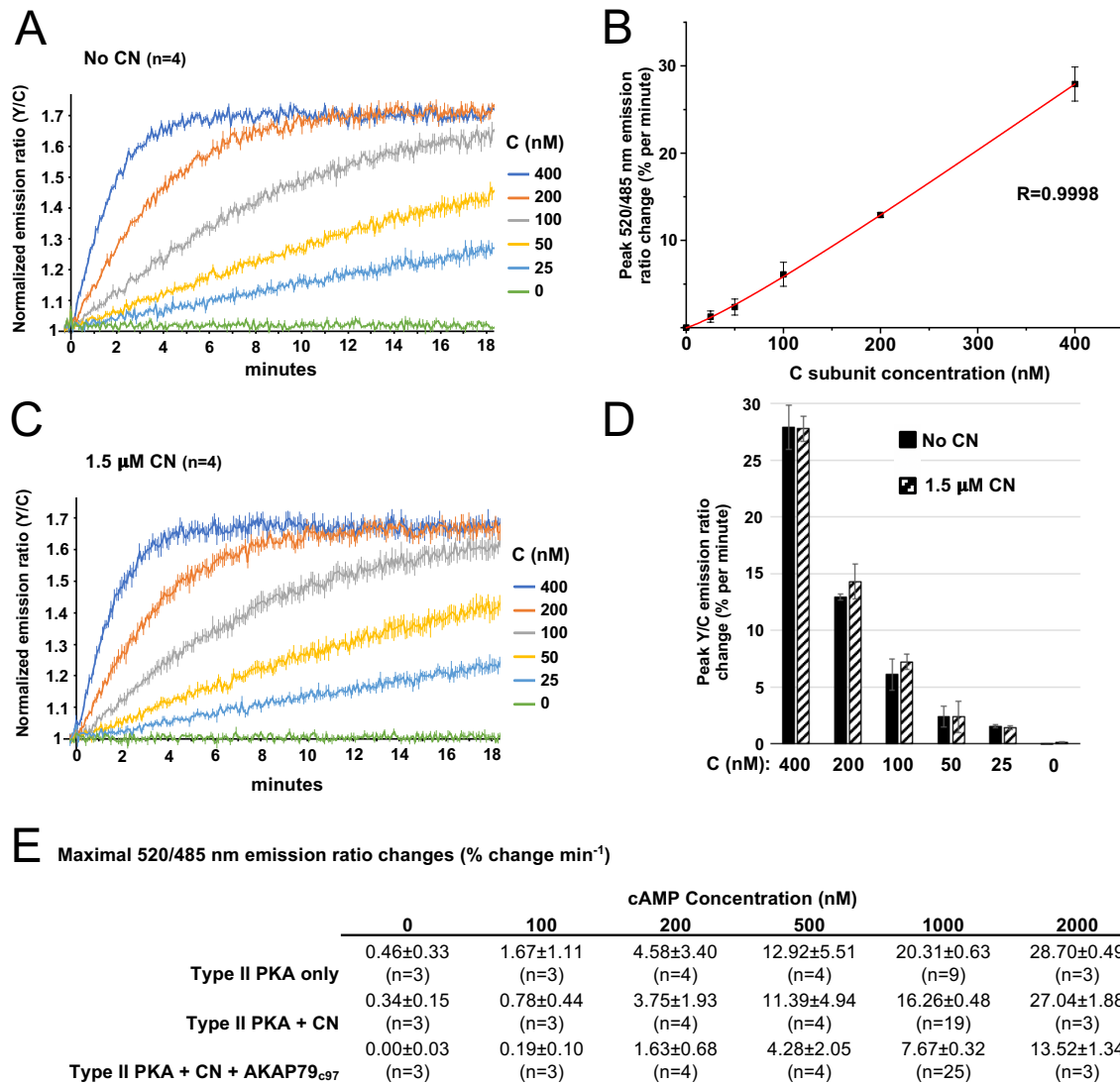
1148 lane, and correspond to the data shown in *Figure 2C*. (A) Anti-pan C immunoblot reference curve. The point

1149 at which the neuropil extract lane falls on the curve is denoted by a green circle. (B) Anti-pan RI reference

1150 curve with neuropil extract lane denoted by a purple circle. (C) Anti-RIIα reference curve with neuropil extract

1151 lane denoted by a light blue circle. (D) Anti-RIIβ reference curve with the neuropil extract lane denoted by a

1152 dark blue circle.



1153

1154

1155

1156

1157

1158

1159

1160

1161

1162

1163

1164

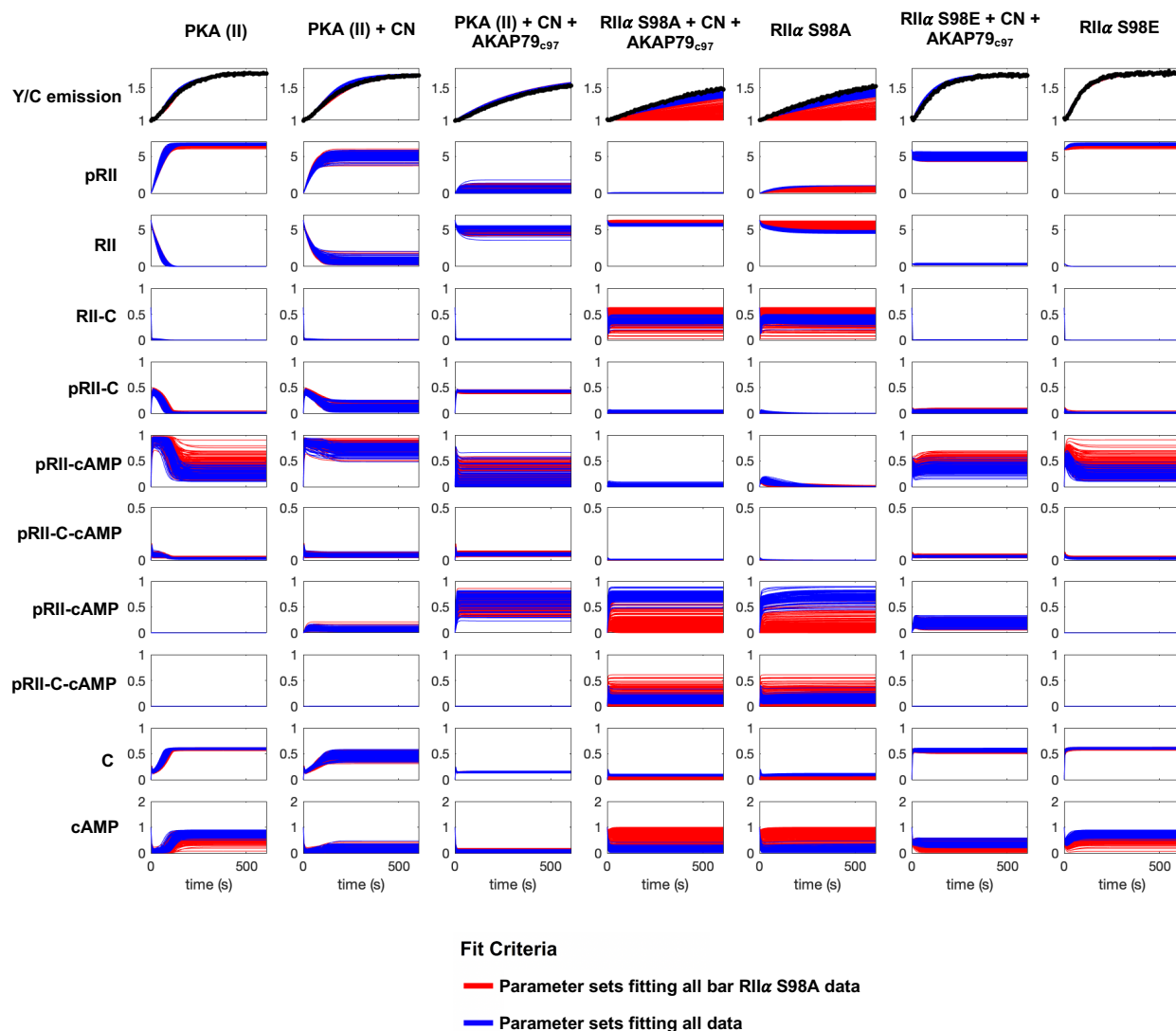
1165

1166

1167

**Figure 3-figure supplement 1. AKAR4 reference measurements with PKA catalytic subunit.** (A) Averaged AKAR4 traces showing change in 520 nm / 485 nm (Y/C) emission ratio over time after injection of 5 mM ATP into reactions containing only PKA C subunits at a range of concentrations. (B) Relationship between free C subunit concentration (in the absence of CN) and emission ratio change per minute. The data was fitted to a Hill function ( $y = 380 \cdot x^{1.71} / (3481^{1.71} + x^{1.71})$ ) with an adjusted R-square value of 0.99983. (C) Averaged AKAR4 traces showing data for the same experiment as the preceding panel but with 1.5 μM CN included in all reactions. (D) Peak 520 nm / 485 nm (Y/C) emission ratio changes at different concentrations of C subunit, either without (black bars) or with (striped bars) 1.5 μM CN. Average rates were calculated between 15-75 s, with the exception of 0 and 25 nM C subunit concentrations (30 – 330 s). (E) Averaged peak AKAR4 responses from all recordings for type II PKA either alone (top row), with CN (middle row), or with both CN and AKAP collected after injections of 5 mM ATP with different concentrations of cAMP. These rates were cross-referenced against the reference curve shown in panel b to estimate free C subunit concentrations (plotted in *Figure 4A-C*). Peak rates were calculated between 30-90 s, with the exception of 0 & 100 nM cAMP responses where a wider time window (30-330 s) was applied.

1168



1169

1170

1171 **Figure 4-figure supplement 1. Simulations of kinetic scheme species changes in concentration over time.**

1172 Each row corresponds to the concentration ( $\mu\text{M}$ ) of an individual species simulated in seven different reaction

1173 mixtures. The first three columns correspond to experiments with WT RII $\alpha$  subunits; columns four and five

1174 to experiments with RII $\alpha$  S98A subunits, and the last two columns with RII $\alpha$  S98E subunits. Red lines correspond

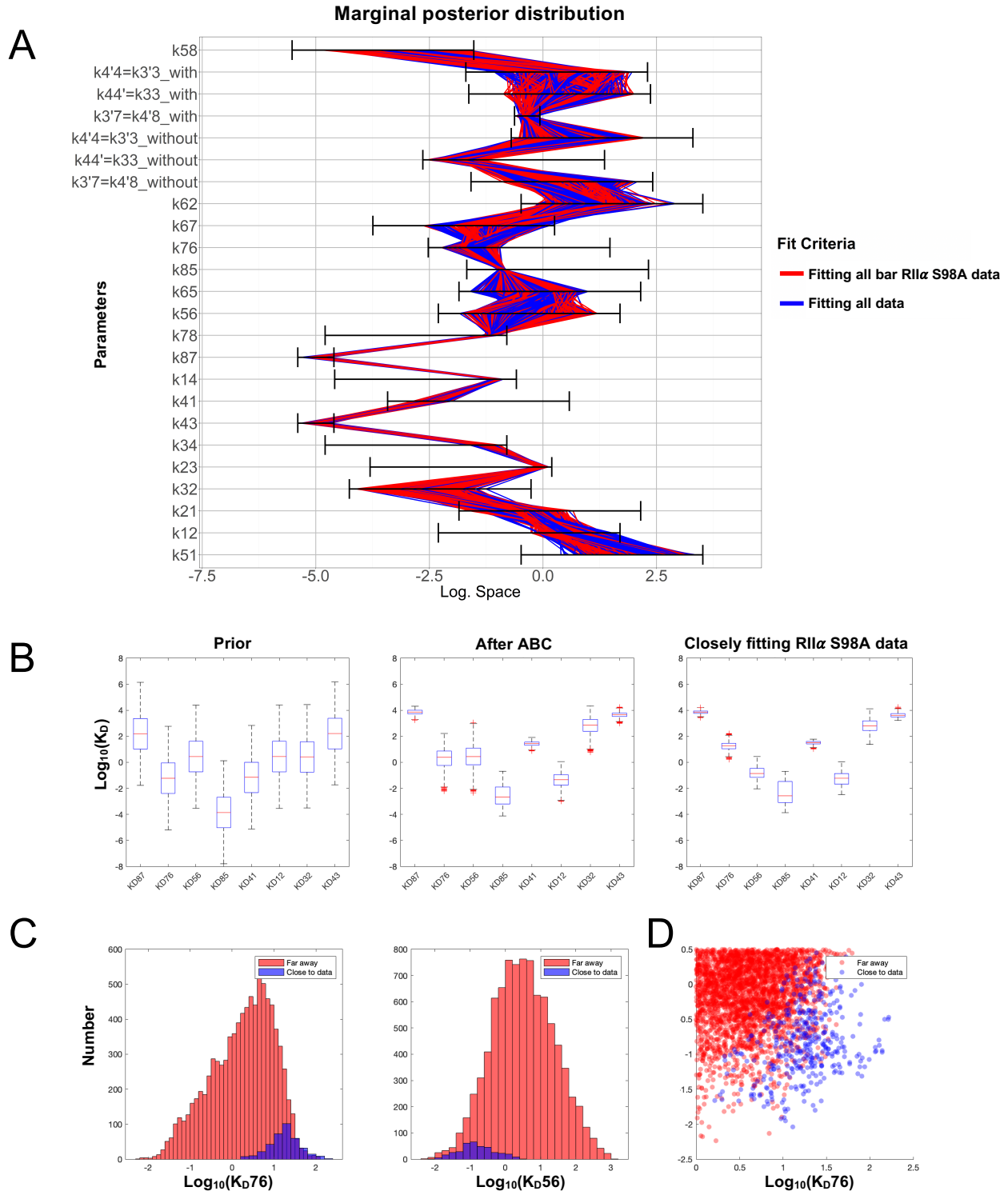
1175 to simulations whose parameter sets were classified as far from experimental data collected with mutated RII $\alpha$ ,

1176 but which fit well to data collected with WT RII $\alpha$  subunits in reactions stimulated with 1 or 2  $\mu\text{M}$  cAMP. Blue

1177 traces correspond to simulations with parameter sets that generated results close to experimental data collected

1178 with both WT and mutant RII $\alpha$  subunits.

1179



1180

1181

1182

1183

1184

1185

**Figure 5-figure supplement 1. Space of parameters used in model fitting.** (A) The illustration shows the marginal posterior distribution of each model parameter on a logarithmic scale for a subset of parameter samples that generated simulations that fit experimental data collected with WT RII $\alpha$  subunits. Each sample in the distribution is connected across the parameters by a line, whose color indicates whether the corresponding

1186 parameter set also generated simulations fitting closely (blue) to data collected with mutant RII $\alpha$  subunits or  
1187 not (red). The parameter priors are indicated by the respective black horizontal bars. It can be noted that the  
1188 following CN-related parameters are always equal:  $k_4'4 = k_3'3$ ,  $k_{44}'=k_{33}'$ , and  $k_3'7=k_4'8$  for each sample.  
1189 **(B)** Distribution of dissociation constants ( $K_D$ 's). The boxplots display median values (red lines), the 50 %  
1190 datapoint distribution around the median (designated by boxes) and the remaining 25% datapoint distributions  
1191 (lower and upper whiskers). Boxplots are shown for all eight  $K_D$ 's obtained with the model priors (left), data  
1192 fitted using experiments with WT RII $\alpha$  subunits (middle), and parameters selected for fitting to data collected  
1193 with RII $\alpha$  S98A subunits. **(C)** Marginal histograms for  $K_{D76}$  (left) and  $K_{D56}$  (right) with parameter sets  
1194 classified according to whether they fit well to the RII $\alpha$  S98A data (blue) or not (red). **(D)** Scatterplot showing  
1195 how the  $K_{D76}$  and  $K_{D56}$  parameters are related according to the same two classes.

1196

1197

1198

1199

1200 **Supplementary Table 1. Kinetic modeling parameters.** The table lists parameters used in computational  
 1201 modeling. Parameters terminology is according to the numbers above states in *Figure 4B*, e.g., k12 refers to  
 1202 the on rate of cAMP binding to state 1 (pRII-C) to produce state 2 (pRII-C-cAMP). The prior range used to  
 1203 initially constrain parameter estimation is provided for each parameter along with links to the references used  
 1204 to define these ranges.  
 1205

Parameter	Value	Parameter Range for ABC	Reference
<b><i>Parameters for phosphorylated RII subunits</i></b>			
k12 (pRII-C + cAMP → pRII-C-cAMP)	0.496 $\mu\text{M}^{-1} \text{s}^{-1}$	4.96e-03 to 4.96e+01 $\mu\text{M}^{-1} \text{s}^{-1}$	(Isensee et al., 2018)
k21 (pRII-C + cAMP ← pRII-C-cAMP)	1.43 $\text{s}^{-1}$	1.43e-02 to 1.43e+02 $\text{s}^{-1}$	
k23 (pRII-cAMP + C → pRII-C-cAMP)	1.56e-02 $\mu\text{M}^{-1} \text{s}^{-1}$	1.56e-04 to 1.56 $\mu\text{M}^{-1} \text{s}^{-1}$	(Zhang et al., 2012)
k32 (pRII-cAMP + C ← pRII-C-cAMP)	5.40e-03 $\text{s}^{-1}$	5.45e-05 to 5.45e-01 $\text{s}^{-1}$	
k43 (pRII + cAMP → pRII-cAMP)	1.0e-05 $\mu\text{M}^{-1} \text{s}^{-1}$	4.0e-06 to 2.50e-05 $\mu\text{M}^{-1} \text{s}^{-1}$	(Ogreid & Doskeland, 1981)
k34 (pRII + cAMP ← pRII-cAMP)	1.60e-03 $\text{s}^{-1}$	1.60e-05 to 1.60e-01 $\text{s}^{-1}$	
k41 (pRII + C → pRII-C)	3.8e-02 $\mu\text{M}^{-1} \text{s}^{-1}$	3.80e-04 to 3.8 $\mu\text{M}^{-1} \text{s}^{-1}$	(Zhang et al., 2015)
k14 (pRII + C ← pRII-C)	2.60e-03 $\text{s}^{-1}$	2.60e-05 to 2.60e-01 $\text{s}^{-1}$	
<b><i>Parameters for dephosphorylated RII subunits</i></b>			
k56 (RII-C + cAMP → RII-C-cAMP)	0.496 $\mu\text{M}^{-1} \text{s}^{-1}$	4.96e-03 to 49.6 $\mu\text{M}^{-1} \text{s}^{-1}$	(Isensee et al., 2018)
k65 (RII-C + cAMP ← RII-C-cAMP)	1.43 $\text{s}^{-1}$	1.43e-02 to 1.43e+02 $\text{s}^{-1}$	
k76 (RII-cAMP + C → RII-C-cAMP)	2.98e-01 $\mu\text{M}^{-1} \text{s}^{-1}$	2.98e-03 to 2.98e+01 $\mu\text{M}^{-1} \text{s}^{-1}$	(Zhang et al., 2015; Zhang et al., 2012)
k67 (RII-cAMP + C ← RII-C-cAMP)	1.80e-02 $\text{s}^{-1}$	1.80e-04 to 1.80 $\text{s}^{-1}$	
k87 (RII + cAMP → RII-cAMP)	1.0e-05 $\mu\text{M}^{-1} \text{s}^{-1}$	4.0e-06 to 2.5e-05 $\mu\text{M}^{-1} \text{s}^{-1}$	(Ogreid & Doskeland, 1981)
k78 (RII + cAMP ← RII-cAMP)	1.60e-03 $\text{s}^{-1}$	1.60e-05 to 1.60e-01 $\text{s}^{-1}$	
k85 (RII + C → RII-C)	2.10 $\mu\text{M}^{-1} \text{s}^{-1}$	2.10e-02 to 2.1e+02 $\mu\text{M}^{-1} \text{s}^{-1}$	(Zhang et al., 2015)
k58 (RII + C ← RII-C)	3.0e-04 $\text{s}^{-1}$	3.0e-06 to 3.0e-02 $\text{s}^{-1}$	
<b><i>Parameters for phosphorylation of RII subunits</i></b>			
k51 (RII-C → pRII-C)	33 $\text{s}^{-1}$	3.30e-01 to 3.30e+03 $\text{s}^{-1}$	(Moore et al., 2003)
k62 (RII-C-cAMP → pRII-C-cAMP)	33 $\text{s}^{-1}$	3.30e-01 to 3.30e+03 $\text{s}^{-1}$	
<b><i>Parameters for dephosphorylation of RII subunits</i></b>			
k44' (pRII + CaN → pRII-CaN)	0.226 $\mu\text{M}^{-1} \text{s}^{-1}$	2.26e-03 to 2.26e+01 $\mu\text{M}^{-1} \text{s}^{-1}$	(Stemmer & Klee, 1994)
k4'4 (pRII + CaN ← pRII-CaN)	20 $\text{s}^{-1}$	2.0e-01 to 2.0e+03 $\text{s}^{-1}$	
k33' (pRII-cAMP + CaN → pRII-cAMP-CaN)	0.226 $\mu\text{M}^{-1} \text{s}^{-1}$	2.26e-03 to 2.26e+01 $\mu\text{M}^{-1} \text{s}^{-1}$	Equal to k44'
k3'3 (pRII-cAMP + CaN ← pRII-cAMP-CaN)	20 $\text{s}^{-1}$	2.0e-01 to 2.0e+03 $\text{s}^{-1}$	Equal to k4'4



$k_{4'8}$ (pRII-CaN $\rightarrow$ RII + CaN)	$2.6 \text{ s}^{-1}$	$2.6e-02$ to $2.6e+02 \text{ s}^{-1}$	(Stemmer & Klee, 1994)
$k_{3'7}$ (pRII-cAMP-CaN $\rightarrow$ RII-cAMP + CaN)	$2.6 \text{ s}^{-1}$	$2.6e-02$ to $2.6e+02 \text{ s}^{-1}$	
<b><i>Parameters for dephosphorylation of RII subunits when AKAP79 is present</i></b>			
$k_{44'}$ -AKAP (pRII + CaN $\rightarrow$ pRII-CaN)	$2.33 \mu\text{M}^{-1} \text{ s}^{-1}$	$2.33e-02$ to $2.33e+02 \mu\text{M}^{-1} \text{ s}^{-1}$	This study
$k_{4'4}$ -AKAP (pRII + CaN $\leftarrow$ pRII-CaN)	$2 \text{ s}^{-1}$	$2.0e-02$ to $2.0e+02 \text{ s}^{-1}$	
$k_{33'}$ -AKAP (pRII-cAMP + CaN $\rightarrow$ pRII-cAMP-CaN)	$2.33 \mu\text{M}^{-1} \text{ s}^{-1}$	$2.33e-02$ to $2.33e+02 \mu\text{M}^{-1} \text{ s}^{-1}$	Equal to $k_{44'}$ -AKAP
$k_{3'3}$ -AKAP (pRII-cAMP + CaN $\leftarrow$ pRII-cAMP-CaN)	$2 \text{ s}^{-1}$	$2.0e-02$ to $2.0e+02 \text{ s}^{-1}$	Equal to $k_{33'}$ -AKAP
$k_{4'8}$ -AKAP (pRII-CaN $\rightarrow$ RII + CaN)	$0.45 \text{ s}^{-1}$	$0.237$ to $0.855 \text{ s}^{-1}$	This study
$k_{3'7}$ -AKAP (pRII-CaN $\rightarrow$ RII + CaN)	$0.45 \text{ s}^{-1}$	$0.237$ to $0.855 \text{ s}^{-1}$	This study
<b><i>Parameters for AKAR4 phosphorylation</i></b>			
AKAR4 + C $\rightarrow$ AKAR4-C	$1.82e-02 \mu\text{M}^{-1} \text{ s}^{-1}$	Fixed	This study
AKAR4 + C $\leftarrow$ AKAR4-C	$0.106 \text{ s}^{-1}$	Fixed	
AKAR4-C $\rightarrow$ pAKAR4 + C	$10.2 \text{ s}^{-1}$	Fixed	

1206  
1207  
1208

1209 **Supplementary Table 2. Oligonucleotide primer sequences**  
1210

Primer Name	Sequence (5' to 3')
EcoI 8HisNLS XbaI	AATTCGCCGGCCACCACCACCACCACCACCACCACGGCGCCCTGCCCCCTGGAGCGCCTGACCCTGTAAT
XbaI 8HisNLS EcoRI	CTAGATTACAGGGTCAGGCGCTCCAGGGGGGGCAGGGCGCCGTGGTGGTGGTGGTGGTGGTGGCCGGCG
XbaI 8HisNLS EcoRI	CTAGATTACAGGGTCAGGCGCTCCAGGGGGGGCAGGGCGCCGTGGTGGTGGTGGTGGTGGTGGCCGGCG
NdeI AKAP79 331	CATGGCAGCCATATGCATCATCACCATCATCATAAAAAGAAATGGAGCCAATTG
NdeI AKAP79 1	CATGGCAGCCATATGCATCATCACCATCATCATATGAGCCACATCCAGATCC
AKAP79 427 EcoRI	ACAGAATCTCCTACTGTAGAAGATTGTTATTTTATTATCATCAGAG
hS98A F	GATTAATAGACGAGTAGCAGTCTGTGCTGAGACC
hS98A R	GGTCTCAGCACAGACTGCTACTCGTCTATTAATC
hS98E F	CTAGCAGATTTAATAGACGAGTAGAAGTCTGTGCTGAGACCTATAACCCTG
hS98E R	CAGGGTTATAGGTCTCAGCACAGACTTCTACTCGTCTATTAATCTGCTAG
ΔPKA F	GAGGATAGAACTTCAGAACAAATATGAAACAAAGAATGCTATTCAGTTGTCAATAGAAC
ΔPKA R	GTTCTATTGACAACTGAATAGCATTCTTTGTTTCATATTGTTCTGAAGTCTATCCTC
Prkar2a F	TAGAATTCCACATGAGCCACATCCAGATCCAC
Prkar2a R	TAGGATCCGAGCTACTGCCCGGGTCCAATAGATC
Prkar2a shRNA resist F	GCGAGGCCCGCCGGCAAGAGTCAGACTCGTTCA
Prkar2a shRNA resist R	TGAACGAGTCTGACTCTTGCCGGCGGCCTCGC
shRIIα F1	GCCAGGAATCAGACTCGTTCATTCAAGAGATGAACGAGTCTGATTCCTGGCTTTTTTGT
shRIIα R1	CTAGACAAAAAGCCAGGAATCAGACTCGTTCATCTCTTGAATGAACGAGTCTGATTCCTGGC
shRIIα 2F	GGAAGCCTGTAAAGACATTTTCAAGAGAAATGTCTTTACAGGCTTCCTTTTTTGT
shRIIα 2R	CTAGACAAAAAGGAAGCCTGTAAAGACATTTCTCTTGAAAATGTCTTTACAGGCTTCC
shRIIα 3F	GGCAGTAGATGTGATGAATTTCAAGAGAATTCATCACATCTACTGCCTTTTTTGT
shRIIα 3R	CTAGACAAAAAGGCAGTAGATGTGATGAATTCTCTTGAAATTCATCACATCTACTGCC
shScram F	GCCACGTCATAGAGACTGTTTCAAGAGAACAGTGTCTCTATGACGTGGCTTTTTTGT
shScram R	CTAGACAAAAAGCCACGTCATAGAGACTGTTCTCTTGAAACAGTGTCTCTATGACGTGGC
rS97A F	CCAGCAAATTTACTAGACGAGTAGCAGTCTGTGCAGAAAC
rS97A R	GTTTCTGCACAGACTGCTACTCGTCTAGTAAATTTGCTGG
rS97E F	CCGATTCAGCAAATTTACTAGACGAGTAGATGTCTGTGCAGAAACGTT
rS97E R	AACGTTTCTGCACAGACATCTACTCGTCTAGTAAATTTGCTGGGAATCGG
RIIα-IRES-EGFP F	GACGAGCTGTACAAGTAAACCGGTGCGGCCGCGACTCTAGATCATAATCAGCCATACCACATTTGTAGA
RIIα-IRES-EGFP R	TCTACAAATGTGGTATGGCTGATTATGATCTAGAGTCGCGGCCGCTGGCCATTTACTTGTACAGCTCGTC
FUGW NheI F	GGCTGCTGGGCTAGCCGGGCTTTC
FUGW NheI R	GAAAGCCCCGGCTAGCCAGCAGCC

1211

1212